Dissolution-precipitation creep in polymineralic granitoid shear zones in experiments II: Rheological parameters

Natalia Nevskaya[1], Alfons Berger[1], Holger Stünitz[2,3], Markus Ohl[4], Oliver Plümper[4], Marco Herwegh[1]

[1]Institute of Geological Sciences, University of Bern; Bern, 3012, Switzerland
5 [2]Department of Geology, Tromsø University; Tromsø, 9037, Norway
[3]Institut des Sciences de la Terre d'Orléans, Université d'Orléans; Orléans, 45100, France
[4]Department of Earth Sciences, Utrecht University; Utrecht, 3584 CB, Netherlands

Correspondence to: Natalia Nevskaya (natalia.nevskaya@unibe.ch)

Abstract. The transition from strong to weak mechanical behaviour in the Earth's continental middle crust is always caused
10 by an initiation of viscous deformation. Microstructural evidence from field examples indicates that viscously deforming polymineralic shear zones represent the weakest zones in the crust and may dominate mid-crustal rheology. The results of recent experiments (as in companion paper 1) demonstrate that the observed weak behaviour is due to the activation of dissolution-precipitation creep (DPC). Formation of fine-grained material and efficient pinning of grain growth are important prerequisites for the formation of a stable deforming microstructure. However, available rheological parameters for fine-
15 grained polymineralic rocks deforming by DPC are insufficient. A series of three types of experiments was conducted on a granitoid fine-grained ultramylonite to different strains at 650°C-725°C, 1.2 GPa with strain rates varying from $10^{-3}s^{-1}$ to $10^{-6}s^{-1}$. Type I and II experiments are solid natural samples, providing key microstructural evidence for DPC. Type III are general shear experiments performed on coarse- and fine-grained ultramylonite powder. All experiments were combined to estimate rheological parameters for such polymineralic shear zones. A stress exponent n≈1.5 and grain size exponent m≈-1.66, with
20 uncertainties, were estimated and coupled with microstructural observations. Extrapolations indicate that at slow natural strain rates, DPC in polymineralic granitoid fault rocks can occur at lower temperatures than monomineralic quartz. A deformation mechanism map is proposed, indicating a transition in the deformation mechanism from dislocation creep in monomineralic quartz to DPC in weaker polymineralic fine-grained granitoid, based on strain rate and grain size. Most importantly, the polymineralic composition is the determining factor in achieving the fine grain sizes necessary for DPC to become activated.
25 This is due to the presence of additional chemical driving potentials and phase mixing, both of which are absent in monomineralic systems.

1 Introduction

In the Earth's middle and lower crust, the switch from frictional to viscous deformation is often accompanied by a transition
30 from seismic to aseismic deformation. Consequently, the study of the onset of viscous deformation in nature is crucial for advancing our understanding of earthquake mechanics. An understanding of viscous deformation in the middle continental crust is of great importance for the amplification of local stresses and the localisation of deep earthquakes, as evidenced by the findings of Campbell et al. (2020).

The rheological behaviour of rocks is commonly estimated from experiments on monomineralic or synthetic simplified rocks.
35 In these experiments, rheology is constrained by intrinsic parameters such as the rock's composition, grain sizes, anisotropies as well as by extrinsic parameters such as temperature, confining pressure, pore fluid pressure and strain rate. Particularly in monomineralic polycrystalline aggregates, two general viscous end member deformation mechanisms are distinguished: Diffusion and dislocation creep, where the former is grain size sensitive (GSS) and latter grain size insensitive (GSI) creep. The Earth's continental crust consists mostly of feldspar-dominated lithologies, which usually are modelled or represented by
40 granitoid rocks. These are a mixture of quartz, feldspars, and micas – among which each mineral has a different temperature for the onset of viscous deformation when deformed in monomineralic aggregates. The initial grain size of granitoids is quite large, ranging from mm- to cm-scale. Of all granitoid mineral phases quartz is considered to be the weakest in monomineralic experiments and typically deforms through GSI creep at grain sizes of the starting granitoid at mid-crustal extrinsic conditions (i.e., greenschist to amphibolite facies P,T-conditions). For this reason, there have been numerous studies to explore GSI and
45 GSS rheology of quartz (e.g. Brok, 1992; Fukuda et al., 2018; Ghosh et al., 2022; Gleason and Tullis, 1995; Hirth et al., 2001; Hirth and Tullis, 1992; Richter et al., 2018; Rutter and Brodie, 2004b, a). Such studies investigating GSS and GSI creep exist also for feldspars (e.g Rybacki et al., 2006, 2008; Rybacki and Dresen, 2000, 2004). Extrapolation to nature indicate that quartz is mechanically weaker than GSI creep of feldspars in the Earth's middle crust. Note that such a generalized statement might not always be true, particularly if GSS creep is the dominating deformation mechanism as is the case for many fine-grained
50 tectonites. Due to observations of GSI in natural monomineralic or coarse-grained rocks the weakest quartz GSI creep is mostly used for modelling crustal strength (Arnold et al., 2001; Brace and Kohlstedt, 1980; Burov, 2003, 2011; Kohlstedt et al., 1995). However, there are many studies of natural rocks indicating that the strength of polymineralic fault rocks may be weaker than predicted by pure quartz GSI creep laws, due to activation of GSS creep mechanisms through continuous grain size reduction (e.g. Fitz Gerald and Stünitz, 1993; Gratier et al., 2013; Stünitz et al., 2020; Stünitz and Fitz Gerald, 1993; Stünitz and Tullis,
55 2001; Wheeler, 1992). To make extrapolations to nature, it is therefore of utmost importance to link the rheology of fine-grained polymineralic granitoid rocks to the formation and evolution of shear zones in the Earth's middle crust.

Few experimental studies exist that attempt to confirm the field observations of polymineralic rocks by investigating the viscous behaviour of fault rocks (e.g. Pec et al., 2012, 2016; Stesky et al., 1974; Sun and Pec, 2021; Tullis et al., 1990; Tullis and Yund, 1977). Many of these experiments use synthetic, initially fine-grained, material as an analogue for fault rocks or

60 pre-cut a rock to simulate a fracture/fault plane. Common conditions for viscous deformation in the lower to middle crust are amphibolite facies (e.g. Okudaira et al., 2010; Pennacchioni and Mancktelow, 2007) but most experiments investigating the viscous processes are conducted at higher temperatures and/or lower pressures to scale natural and experimental conditions (see compilation of high temperature quartz experiments in Ghosh et al., 2022).

Our aim is to understand the rheology of polymineralic fine-grained shear zones in the Earth's middle to lower crust. This is

65 why in this study we deform a natural, initially fine-grained granitoid ultramylonite at 650-725°C, 1.2 GPa confining pressure and shear strain rates of 10^{-3} to 10^{-5} s^{-1}, general strain rates of 10^{-6} s^{-1}. To capture the complexity of natural samples, we use three different experimental geometries for this mylonite. Our setup allows to reach fairly high strains at experimental conditions and activate viscous deformation in polymineralic fine-grained zones even at faster strain rates than observed in other coarse granitic or monomineralic studies (see companion paper 1). We investigate the importance of grain size reduction

70 leading to substantial weakening of polymineralic rocks. In this present study, we estimate the parameters describing stress and grain size sensitivity for a flow law to finally compare to literature data and to extrapolate the experimental findings and observations to shallower crustal levels. Our results have direct implications for the onset of viscous deformation and rheology of polymineralic shear zones.

2 Materials and methods

75 ### 2.1 Starting material characterization and preparation

This study has been performed on a granitoid ultramylonite from the Central Aar granite in the central Alps. Peak metamorphic conditions of this ultramylonite were estimated at 450°C and 600 MPa (Challandes et al., 2008; Goncalves et al., 2012). The structures were not overprinted afterwards, leaving the original mylonitic structures unmodified. Coring from an underground test laboratory (Grimsel test site) provided fresh sample material devoid of any weathering features.

80 The granitoid ultramylonite consists of quartz, feldspars, biotite, and epidote. It is strongly foliated through mylonitic bands (qtz:ab:K-fsp:bt:ep = 37:38:11:8:6 wt%). Mylonitic bands were carefully investigated and characterized. Bands are ~100-400 μm wide and have varying mineralogical composition and grain size (see companion paper 1). Microstructural analysis of the starting material has been performed on thin sections in a petrographic microscope as well as SEM. The mylonitic bands have a grain size range of <10 μm (even down to 2 μm) to >600 μm in proto-mylonitic zones. The most fine-grained and

85 homogeneous zones with a median ~15 μm were targeted for our experiments. In such zones micas are well mixed with feldspars, quartz, and epidote.

2.2 Deformation experiments

We deformed the granitic ultramylonite in a Griggs type apparatus at the University of Orleans at confining pressures of 1.2 GPa and temperatures between 650°C and 725°C. We used three different experimental setups, in which the samples were

90   deformed at varying strain rates and to different strains. These different types of experiments bring different insights to strain
      evolution and deformation mechanisms, that can be used for extrapolation to nature (see Fig. 1):

- **Type I:** Shear experiments using natural samples, where strain localization in fractures results in dominant simple shear deformation.

95   - **Type II:** Coaxial shortening experiments using natural samples where deformation is more homogeneously distributed.

- **Type III:** General shear experiments using coarse-grained (cg) and fine-grained (fg)
100   powders obtained from a natural sample between alumina pistons.

All three experiments were performed on the same starting material, only the sample preparation was different. For Type I and II, the ultramylonite was cored
105 with a 6.3 mm diameter diamond drill, such that the foliation is inclined 45° with respect to the piston axis. These cylindrical samples were carefully investigated macroscopically and with a micro-CT Scan (Skyscan)

Figure 1: Schematic of the three experimental Types in this study. Details see text.

prior to experimental deformation to ensure that a most homogeneous and fine-grained zone is targeted, as well as no drilling-
110 induced fractures exist. For Type III, one portion of the ultramylonite has been disintegrated using the inhouse SELFRAG Lab
      (high voltage pulse machine, https://www.selfrag.com/; (Edwin et al., 2006; Regis et al., 2014)) and further milled by hand
      and in a ball mill (McCrone corundum ball mill). Material from each step was sieved several times to obtain grain sizes below
      125 μm, maximizing disintegrated grains and minimizing damage of grains from the milling process. This material was used
      directly for Type III-cg (cg: coarse grained) experiments. From this milled sample batch, a small part has been used to perform
115 XRD measurements to obtain a chemical composition of the bulk rock material. For Type III-fg experiments (fg: fine grained),
      a second batch of powder was prepared by milling the <125 μm samples with the McCrone mill and further by hand. After
      several milling cycles, Atterberg cylinder sedimentation was performed to separate a fraction < 2.8 μm. For sedimentation
      times, T_{room}=19.9°C (climatized), column height = 28 cm, particle density 2.75 g/cm^3 and suspension medium H_2O was
      considered. The grain size distribution of the gouge samples was measured by laser diffraction in a Mastersizer 3000 (see
120 distribution in supplementary). To avoid clustering in the clay grain size fraction, the dried powder with a droplet of ethanol
   was homogenized with a pestle and mortar until dry again.

Brittle fractures in sample Type I experiments typically are formed before reaching experimental P,T-conditions. We term these cataclastic shear zones in a coherent sample as pre-fractured microstructures. The grain sizes are reduced in a brittle manner down to <0.5 μm from initially ~15 μm. One benefit of the Type I experiments are the large shear strains that can be

125   obtained in the thin zones (up to $\gamma = 200$), resulting in microstructures that are close to steady state conditions (see also microstructures in companion paper 1). Furthermore, these zones simulate the evolution of natural faults from brittle to viscous behaviour. In literature, this type of experiments has rarely been used for mechanical tests so far because of its difficult corrections of the stress measurements. Exceptions are the experiments of Stesky et al. (1974) and Tullis et al. (1990) but some experimental conditions were different (mostly frictional properties in case of Stesky et al. (1974)). Most importantly, their

130   shear stress and shear strain rate were calculated in a different manner compared to our approach (see Section 2.3.4, Correction of raw data). Type II samples represent a more common setup of coaxial shortening experiments and can be used reliably to understand strain evolution and deformation mechanisms (Dell'Angelo and Tullis, 1988; Ghosh et al., 2022; Stipp and Tullis, 2003). Type III experiments represent a commonly used Grigg's rig simple shear set up (Fukuda et al., 2018; Okazaki and Hirth, 2016; Stünitz and Tullis, 2001). These experiments are affected by boundary conditions such as friction of the forcing

135   blocks against the actuator, compaction of initial porosity, and maximum possible shear strain/ gamma values of 3-4. Type III experiments, however, allow to compare the influence of different starting grain sizes (<2.8 μm and <125 μm in our case), as well as to perform strain rate and temperature stepping with a controlled sample geometry and grain size. As will be shown below, the extraction of microstructural and mechanical information benefits from the use of all three approaches.

2.3 Grain size analysis

140   Coarser grained microstructural domains (>~1 μm) were mapped with a small (500-1000x) magnification on stitched SEM images, where the image sequence was taken as a cross section perpendicular to the shear zone. For the small scale (~1000-50 nm), grain sizes were measured on high (5000-30 000x) magnification FEG-SEM backscatter electron detector images by drawing the grain boundaries manually. Automated image analysis techniques would have required larger datasets to be trained on, as well as better defined grain boundaries. However, in our samples, these conditions were not met and for each grain it

145   was decided manually whether it is a grain or not. This method was limited to areas, where phases were mixed, because many grain boundaries were not visible in monophase regions. More reliable and smaller scale grain size analysis (~500-10 nm) was performed on TEM-sections. This validation shows that FEG-SEM images were sufficient to resolve grain sizes that were confirmed through TEM down to <50 nm. Number-weighted densities and medians from outlined grains in FiJi ImageJ were calculated for large and fine grain sizes by calculating the diameter d of the area A of equivalent circles:

150   $$d = 2 \cdot \sqrt[2]{A/_\pi} \; ; \; Med(d) \; , \tag{1}$$

5

This workflow allows capturing the broad range of grain size distributions from nm to µm scale in our experimentally deformed samples, where grain size reduction at grain boundaries and initial grain size influence the strength equally, as will be shown below.

Limitations of resolution in regions of extremely fine-grained material and restriction to observations of phase boundaries
155 instead of grain boundaries (measuring several grains as a single one) will result in an upper limit of the actual grain sizes (e.g. Berger et al., 2011; Heilbronner and Keulen, 2006). Hence the median of corresponding ranges will overestimate the grain sizes and should be used with caution. Despite these limitations it is demonstrated that in our experiments grain sizes are reduced by orders of magnitude from the starting material, which results in robust grain size data making it possible to draw conclusions about the shear zone evolution.

160 **2.4 Corrections of raw data**

In terms of mechanical data, each type of experiment requires different corrections for different sample geometries. In Type I experiments, the shear strain rate is calculated from the thickness of the zone and the vertical displacement of the piston depending on the angle of the shear zone with the shortening direction. It is a standard procedure resulting in shear strain rates $\dot{\gamma}$. Conversion of shear strain rates of the Type I and Type III experiments to equivalent strain rates $\dot{\varepsilon}_{eq}$, is done by following
165 Eq. 2 (as in e.g. Kohlstedt and Hansen, 2015; Sun and Pec, 2021):

$$\dot{\varepsilon}_{eq} = \dot{\gamma}\frac{2\cdot\sqrt{3}}{3}, \tag{2}$$

Note that this $\dot{\varepsilon}_{eq}$ is considered directly comparable with the calculated $\dot{\varepsilon}$ of Type II experiments.

In Type I and Type III experiments differential and shear stress are calculated, in Type II experiments differential stress is calculated. While in shear zones forming at 45° a conversion from shear stress to differential stress is simple by a factor of
170 two, the shear stress for other angles α of the shear zone is calculated as in Eq. 3:

$$\tau_\alpha = \frac{\sigma_D}{2\cdot\sin(2\alpha)} \text{ or equivalently } \sigma_D = \tau_\alpha \cdot 2 \cdot \sin(2\alpha) , \tag{3}$$

To capture the complexity of our experiments, we used equivalent strain rate $\dot{\varepsilon}_{eq}$ paired with angle-dependent shear stress τ_α for our stress exponent calculations. Comparison with differential stress calculations shows that the calculated values for stress and grain size dependence do not change significantly for the observed range of values. For comparison with literature data,
175 we therefore use differential stress for stress dependence, as the equivalent shear strain rate already contains the shear zone angle.

Additionally, corrections of the Grigg's type apparatus internal friction were performed and furthermore a friction increase of 1.3 kN/mm subtracted from the load data (see calibrations and "friction correction" by Pec (2014) and Tarantola et al. (2012)). As the samples are very fine-grained, compaction occurs very early during the experiment (during pressurization and very
180 early in the slope section of the loading curve), and a compaction correction is neglected, to reach γ values similar to the ones measured in the thin section by hand. A detailed description of the different calibrations and corrections can be found in

Holyoke and Kronenberg (2010), Pec, (2014), Tarantola et al. (2012). The uncertainty resulting from the different corrections is displayed in Fig. 2. The HK molten salt cell correction (Holyoke and Kronenberg, 2010) was tested on the dataset, and we found the calculated parameters did not change significantly (see supplementary). However, as we use a solid salt cell, this

185 correction would require subtraction of another 48 MPa which would lead to negative differential stress values at slow strain rate steps of Type III experiments. This would imply extension experiments, which were not performed, and therefore we do not implement the Holyoke and Kronenberg correction to our experiments. Stresses are shown as only friction corrected without any further corrections applied.

During shear experiments, the area on which the force acts changes continuously and the recorded load data must be corrected

190 for obtaining shear stress values. In the case of localized shear zones, in Type I and III experiments, there is a decreasing overlap area resulting in increasing stress values with progressive shear strain. We use the $\cos^2$-approximation for the decreasing overlap area for Type III experiments (Heilbronner et al., 2020). In the case of Type I experiments, the strain is beyond the applicability of this correction (should only be applied up to $\gamma<4$, Stünitz & Heilbronner, personal communication) and the correction is therefore omitted. During coaxial shortening, barrelling of the sample occurs and leads to an increased

195 cross-sectional area on which the force acts. We assume constant volume to correct Type II experiments for the increasing area with a Poisson ratio correction of 0.5, as described by Pec (2014). This effect is not considered in the correction of in Type I experiments, where we use only the friction corrections. A compilation of different corrections and their effect on the mechanical data can be found in Fig. 2.

A major uncertainty of our Type I experiment samples is their geometry. We assume that the defined zone deforms

200 homogeneously rather than as a composite of deformation events and different rates and measure its width in a transect in the centre of the sample perpendicular to the shear zone. We measure an averaged shear zone width at several points of the cross-section and use this value for calculations. The calculated shear stress is not affected by this error. However, it does influence the shear strain rate significantly (see Supplementary): A 10-fold increase of shear zone thickness (e.g. from 10 to 100 µm) leads to a 1000-fold slower calculated strain rate. This highlights the importance of the Type III experiments to have a reliable

205 stress and strain rate measure.
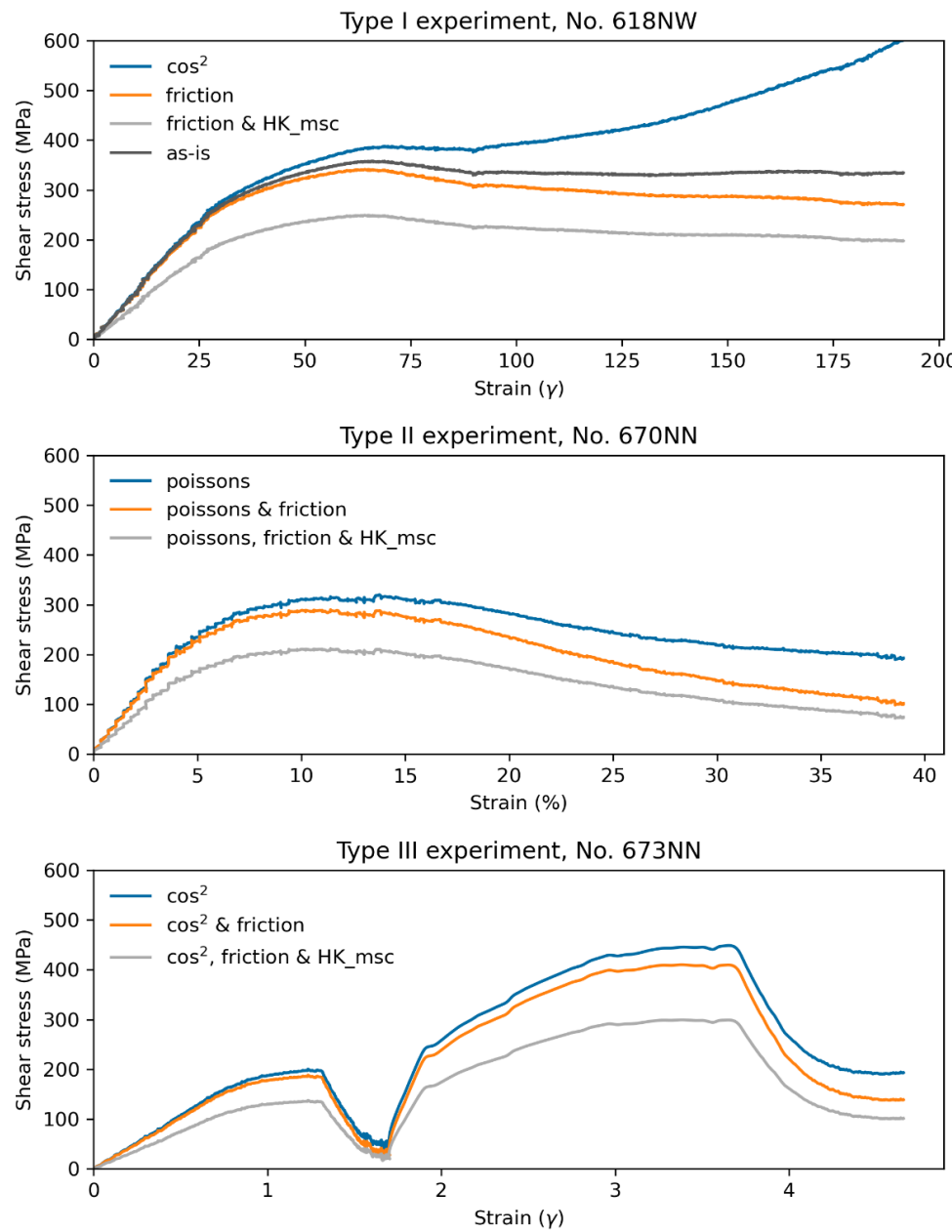
Figure 2: Different corrections for recorded data. For more details on each correction see text. Abbreviations: as-is=only corrected for the stiffness of the machine etc, no geometric corrections; cos²= cosine squared correction developed by R. Heilbronner; friction = additionally, machine friction was corrected; HK_msc=Holyoke & Kronenberg (2010) correction as for a molten salt cell (modified slope, no modification of offset); poissons = corrected for the poissons ratio.

2.5 Extrapolation parameters

To be able to extract the parameters determining the strength of our samples across all experimental conditions and geometries,

210   we use the constitutive equation of a common diffusion (GSS) creep flow law (Eq. 4):

$$\dot{\varepsilon}_{eq} = A\,\sigma^n d^{-m} exp^{\left(-Q/RT\right)} ,$$
(4)

Where $\dot{\varepsilon}_{eq}$ is the equivalent strain rate in s^{-1}, σ the differential stress in MPa with stress exponent n, d the grain size in μm with stress exponent m, Q the activation energy in J/mol, T the temperature in K, R the universal gas constant and A a pre-exponential term in MPa^{-n} μm^{m} s^{-1}. We chose the general form of a grain size sensitive (i.e. diffusion creep) flow law, as the

215   inferred deformation mechanism in companion paper 1 is grain-size sensitive dissolution-precipitation creep and aim to correlate the microstructural observations with mechanical data.

To estimate the exponential factors n, m and Q in this Eq. 4, linear regression fits are made in log$_{10}$ plots for each modified parameter (see sections 3.2, 3.3 and 3.4). The stress exponent is the most important parameter for inferring deformation mechanisms and for extrapolation to natural conditions, because it is the best constrained parameter, as will be shown below.

220   The grain size exponent and subsequent parameters are only to be taken as rough estimates rather than precise measurements. Nevertheless, they serve as a guideline for natural conditions close to our experimental conditions and as a parameter for comparison with literature data.

9

Table 1: Summary of experimental parameters. The shear strain rates are calculated from final shear zone thicknesses after the experiment, as described in the text.

| Exp. No.	Type	Diameter (mm)	Initial height (mm)	P+T conditions	Water (H2O)	Vertical strain ε (%)	Shear strain γ (final)	Final shear zone thickness (mm)	Shear zone angle (°)	Coaxial strain rate (s⁻¹)	Shear strain rate (s⁻¹)	Equiv. strain rate (s⁻¹)
633NN	I	6.07	12.33	1.2GPa, 650°C	0.2wt%	7.0%	103	0.010	35	8.96E-07	1.34E-03	1.55E-03
632NN	I	6.07	12.30	1.2GPa, 650°C	0.2wt%	5.0%	54	0.030	38	6.47E-08	6.82E-05	7.88E-05
635NN	I	6.09	12.19	1.2GPa, 650°C	0.2wt%	10.0%	46	0.030	39	1.10E-05	5.77E-03	6.66E-03
631NN	I	6.10	12.24	1.2GPa, 650°C	0.2wt%	5.0%	75	0.010	35	1.04E-06	1.56E-03	1.80E-03
618NW	I	6.11	12.30	1.2GPa, 650°C	0.2wt%	27.5%	191	0.020	42	1.29E-06	1.07E-03	1.23E-03
630NN	I	6.10	12.42	0.15GPa, 100°C	0.0wt%	0.0%	—	—	—	—	—	—
634NN	II	6.08	12.27	1.2GPa, 650°C	0.2wt%	0.0%	—	—	—	—	—	—
670NN	II	6.16	12.34	1.2GPa, 650°C	0.2wt%	40.0%	—	—	—	1.34E-06	—	—
669NN	II	6.16	12.65	1.2GPa, 650°C	0.2wt%	5.0%	—	—	—	1.26E-06	—	—
658NN	II	6.18	12.33	1.2GPa, 650°C	0.2wt%	6.8%	—	—	—	1.13E-06	—	—
662NN	II	6.15	12.45	1.2GPa, 650°C	0.2wt%	8.0%	—	—	—	1.11E-06	—	—
673NN	III-fg	6.33	—	1.2GPa, 650°C	0.1wt%	—	1.2			—	2.91E-04	3.36E-04
							1.7	0.664	45		4.52E-05	5.22E-05
							3.6				3.07E-03	3.55E-03
							4.6				3.96E-04	4.58E-04
675NN	III-cg	6.33	—	1.2GPa, 650°C	0.1wt%	—	3.8			—	6.06E-04	6.99E-04
							4.4	0.538	45		5.83E-05	6.73E-05
							4.6				1.13E-05	1.31E-05
							7.1				5.07E-04	5.86E-04
677NN	III-fg	6.33	—	1.2GPa, 725°C	0.1wt%	—	3.6			—	4.66E-04	5.38E-04
							4.1	0.475	45		4.85E-05	5.59E-05
							5.4				4.78E-03	5.52E-03
							6.9				4.89E-04	5.65E-04

3 Results
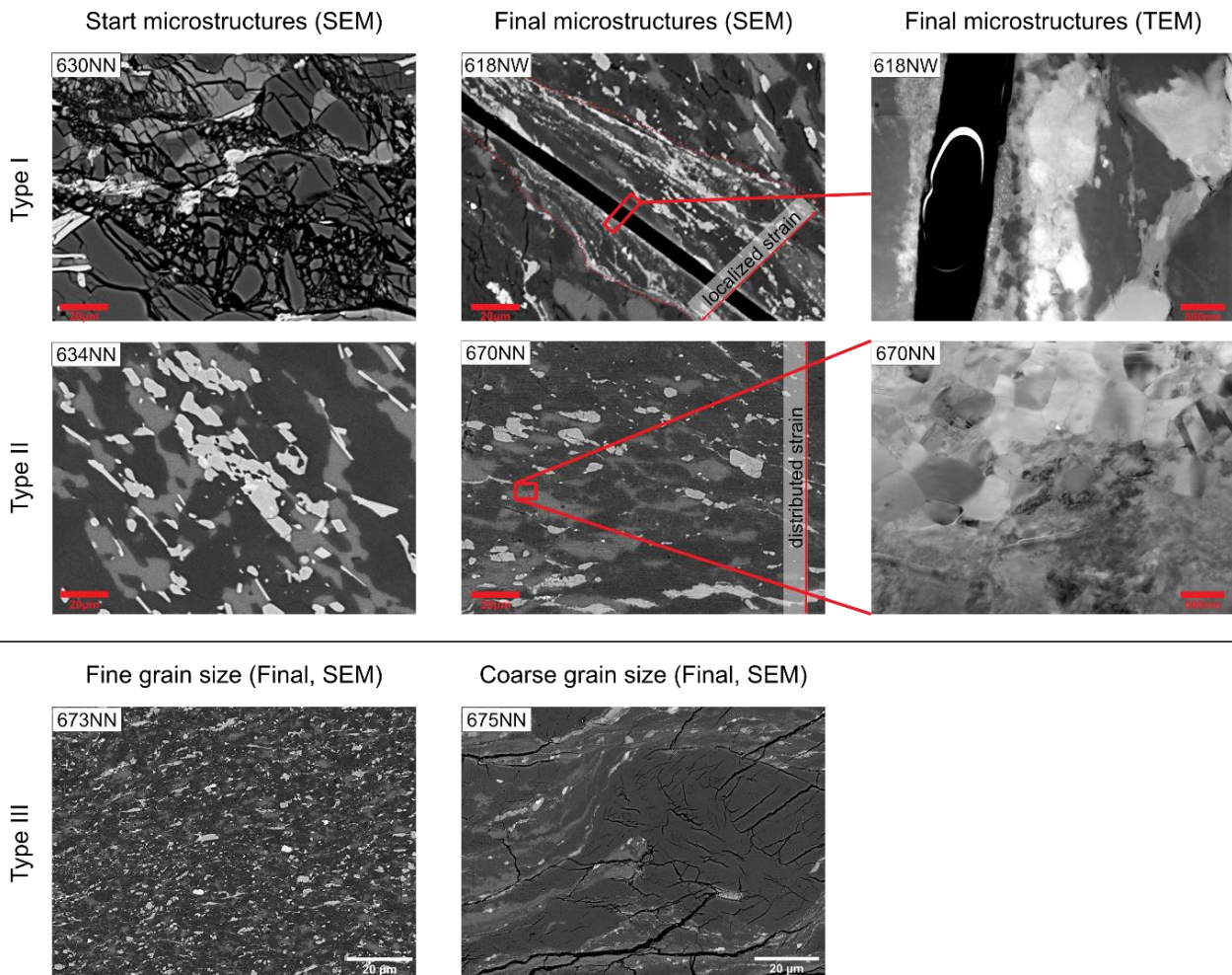
Figure 3: Summary of starting and steady-state key microstructures highlighting the different experimental geometries as well as strain localization mechanisms of all three experimental types. For Type III, only final microstructures were investigated. All SEM images were recorded using the backscatter electron detector: Bright phases: bt&ep, medium grey phases: K-fsp, dark grey phases: ab+qtz. Note the same scale in the first two columns. Type I TEM section is a vertical slice through the highest strain zone with an unloading crack in the middle. Type II TEM shows the phase boundaries between ab (top) and K-fsp (bottom). Type III highlights the homogeneous strain and grain size distribution for a fine starting grain size and a bimodal grain size distribution for a coarse starting grain size, with a big quartz grain in the center. Note the very similar grain size in the fine-grained area of the coarse experiment and the fine-grained experiment.

3.1 Strain rates and grain sizes

We performed 14 relevant experiments in total, of which 6 Type I, 5 Type II, and 3 Type III experiments at shear strain rates of 10^{-3} to 10^{-5} s^{-1}, coaxial strain rates of 10^{-6} s^{-1} (see Table 1). The shear strain rates were calculated based on final shear zone thickness measurements after deformation. Figure 3 summarizes the microstructures serving as a base for our interpretations

11

(see more details for microstructures in companion paper 1). Two samples were loaded and unloaded without deformation to
compare the starting microstructures: One with a fracture created at 100°C and 1.5 kbar, one without a fracture and set to
experimental P/T (650°C, 1.2 GPa) over-night (630NN and 634NN respectively, see Table 1 and Fig. 3).

In Type III experiments, we performed strain rate stepping and the final shear zone width varied between 475 and 664 μm.
Each of the experiments were deformed with 4 strain rate steps – always one order of magnitude faster/slower than the previous.
We used a one magnitude slower strain rate for the coarser starting material experiment (unlike in the fine-grained material)
since a fast strain rate of $10^{-3}s^{-1}$ led to high differential stresses causing jacket rupture (see all experimental parameters in
Table 1, all experiments in Fig. 4).The first and last strain rate steps were set to the same speed, to test for stable microstructures
and mechanical data over all strain rate steps. In Type III-fg experiments, after reaching a peak shear stress the samples directly
deformed at steady state stress; in Type III-cg, weakening occurred at the first strain rate step before reaching a steady state
flow stress (Fig. 4.). In Type III-fg, the whole zone deforms homogeneously. Type III-cg is inhomogeneous, shows strain
partitioning and a bimodal grain size distribution (see Results, Fig. 7).

In Type II experiments, we calculate the bulk strain as a coaxial shortening strain. It is observed that typically the lower 1/3 to
2/3 of the sample are deformed, whereas the upper part remains weakly or undeformed (schematic in Fig. 1). These samples
show a continuous weakening (see Fig. 4) and do not reach steady-state conditions.

In Type I experiments, the angle of the shear zone to the shortening direction varied between 35° and ~42°, the maximum
thickness of the localized zone was 0.01 to 0.02 μm. In each case, the preexisting mylonitic fabric is not exploited as a
deformation fabric despite its favourable orientation for shear. The stress recording shows a peak stress, then slight weakening
and reaching nearly steady-state conditions after a shear strain of gamma ≈70 (Fig. 4). One sample (630NN) was pressurized
to brittle failure, to obtain the starting microstructures before reaching experimental P,T-conditions. A slow strain rate
experiment (632NN) lasted only until peak stress and is therefore not considered for the flow law calculations.

In addition, in Type I experiments the shear zone evolution was considered and (shear) strain rate calculations therefore were
carried out after microstructural observation (companion paper 1) and measurements of the shear zone width. We use
observations from the shear zone evolution in terms of shear stress and strain localization for shear zone widths and
corresponding grain sizes (see Fig. 5). As described in companion paper 1 (and summarized in Fig. 5), the deformation starts
with a wider shear zone (20 μm) and coarser grain size (median ~150 nm) at peak stress, and subsequently localizes in narrower
(2 μm-200 nm), extremely fine-grained (median 53-13 nm) and slightly weaker zones at ~steady state stress. All grain size
ranges are assumed to be preserved in the final microstructures (companion paper 1). At the same time, the shear zone is
localizing and further narrowing (Fig. 5), hence at constant vertical displacement rate, the actual strain rate becomes
incrementally faster. These values give the range for strain rates with corresponding stresses and the grain size sensitivity.

The grain sizes in Type III-fg experiments as well as peak stress of Type I and high strain regions of Type III-cg develop
towards similar grain-size median values ranging from ~145 to ~250 nm. Type II experiments exhibit a bimodal grain size

distribution (similar to Type III-cg), where newly formed grains occur at phase boundaries of feldspars. There, we observe median grain sizes of 270 nm in the boundaries of starting feldspars, with a range of 58-808 nm.

We repeated experiments at the same conditions but to different strains to show the reproducibility and understand the geometric, mechanical, and microstructural evolution of the samples (see Fig. 4). In the following, we show that the data is

265   consistent despite the natural complexity of the starting material and the use of different experimental setups.
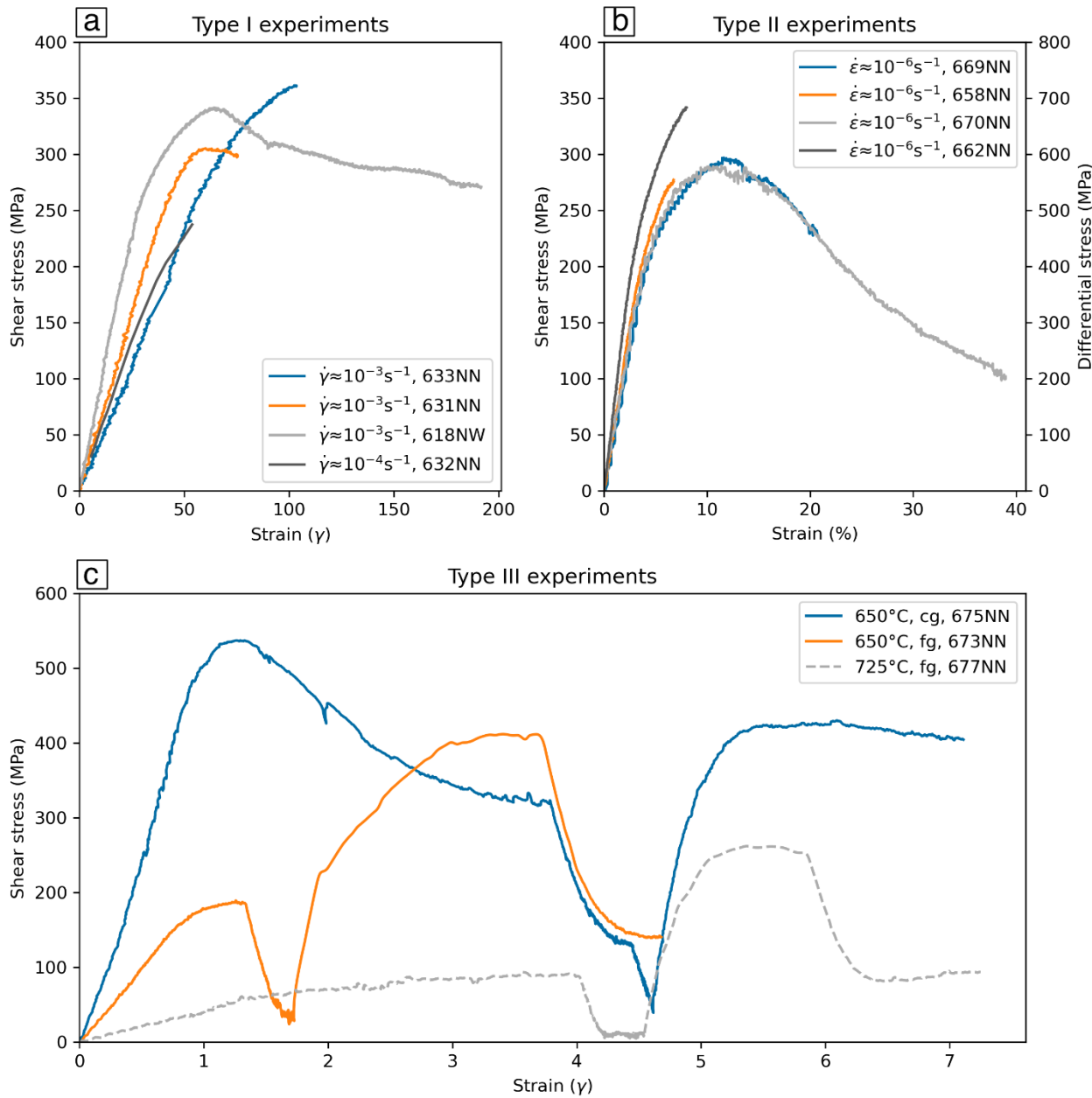
Figure 4: Experiments, which are used in this study, as stress-strain diagrams. Corresponding experimental parameters can be found in Table 1. Note that for Type I experiments (a), the initial slope appears not to match, however, this effect is caused by the different shear zone widths leading to different strain calculations at same vertical displacements. Type II experiments (b) were all performed at the same conditions to different strains. Slight variations in peak stress may be due to compositional changes. Type III experiments (c) are performed with fg = fine grained; cg = coarse grained material, varying temperature and with strain rates in steps. As a result, each increment in the slopes is caused by a change of strain rate according to the rates in Table 1.
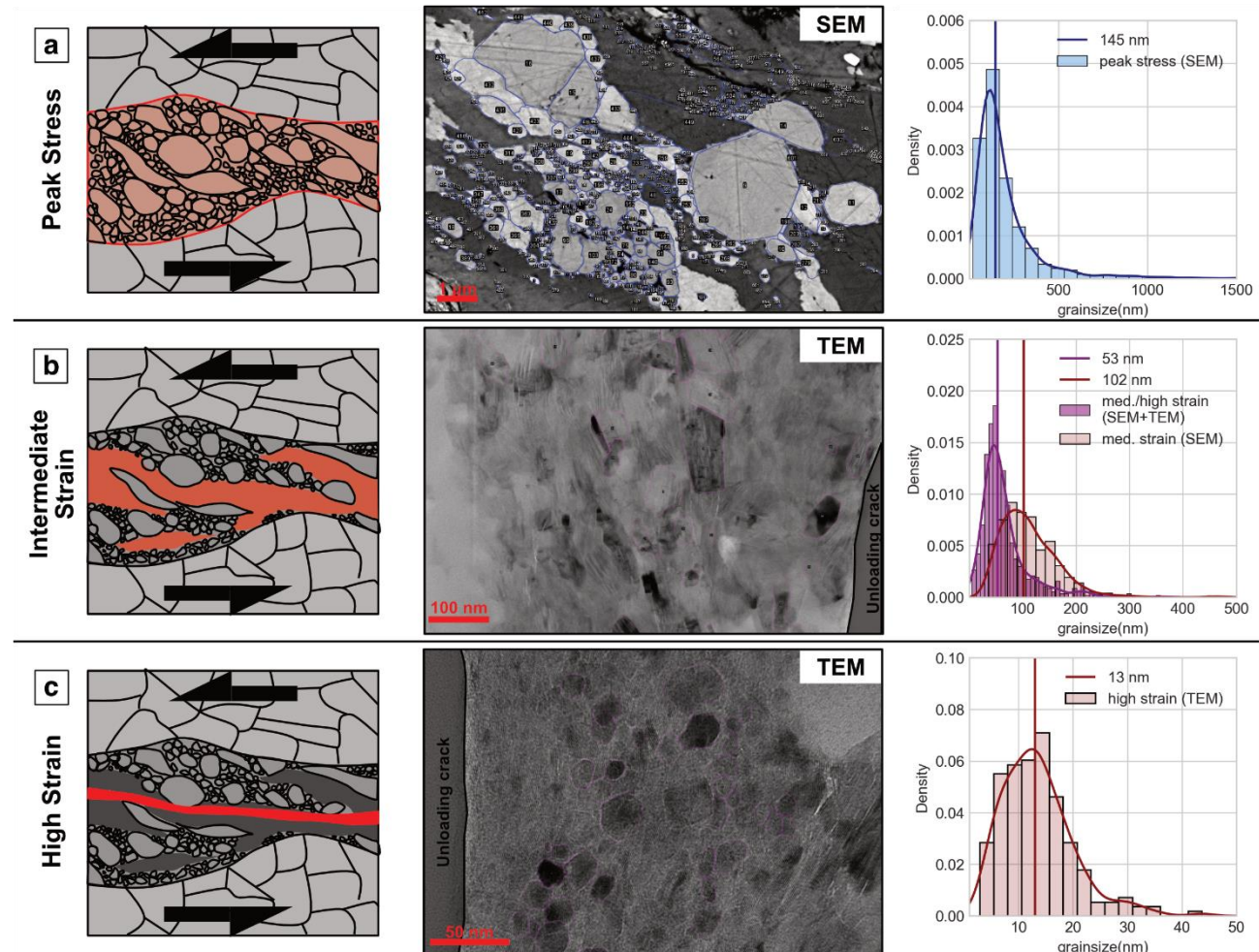
Figure 5: Shear zone evolution in terms of strain localization and grain sizes for experiment 618NW as an example of Type I experiments. Red in the schematic is the distribution of deforming zone. Note the varying scale for the grain size distribution, which was chosen to display the dramatic grain size reduction from peak stress to high strain/steady state stress zones. Blue and pink lines in the SEM/TEM images are manually drawn for grain size measurements in Fiji ImageJ. The Grain size distributions compile measured grains not only from the displayed images, but similar comparable microstructural domains.

270
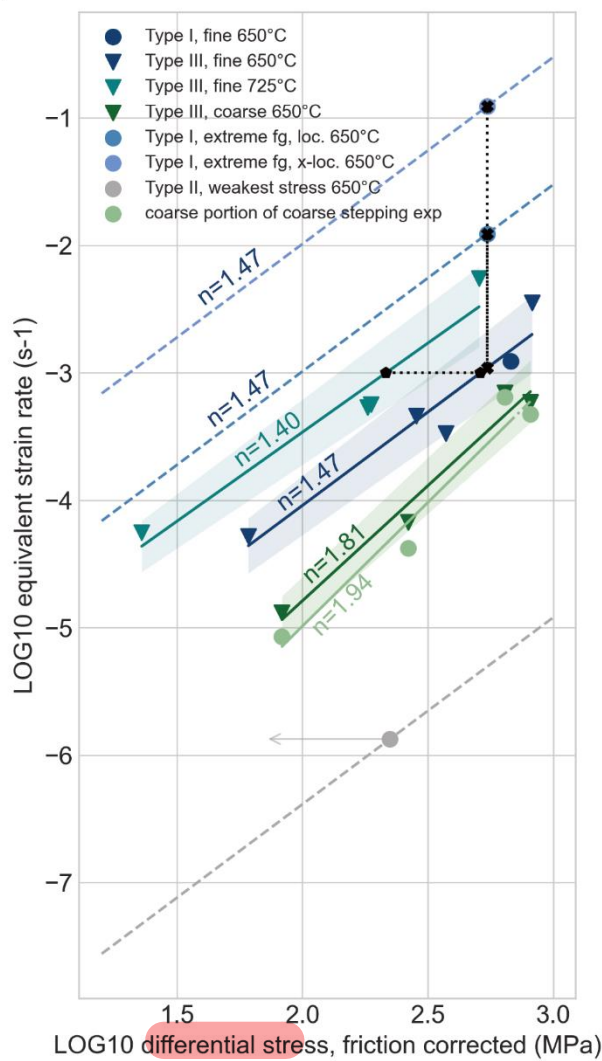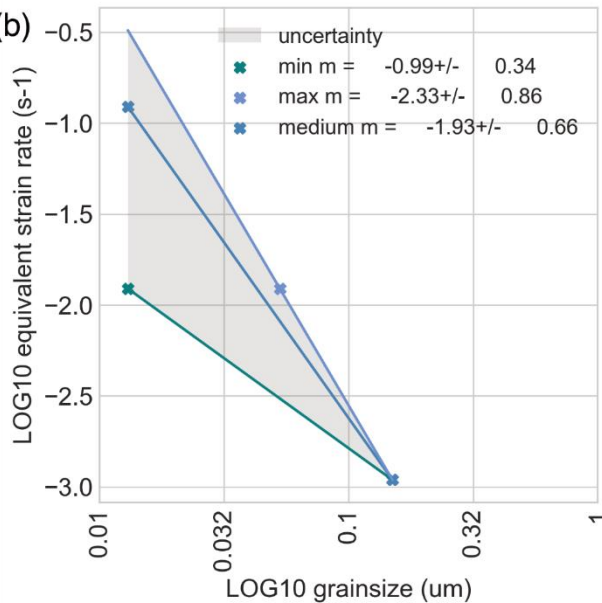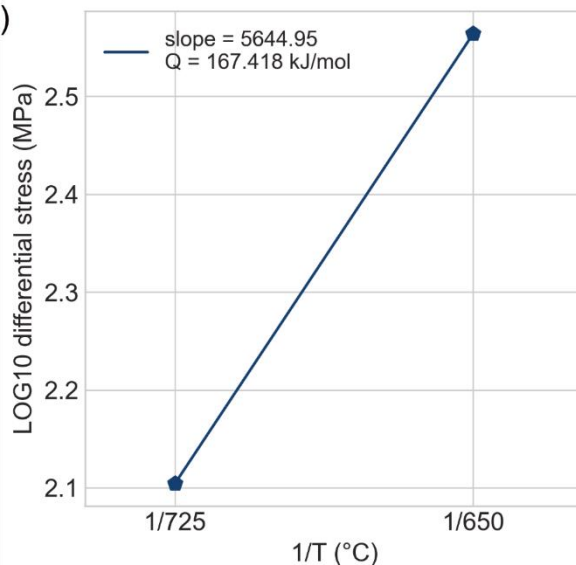
Figure 6: Calculations of rate, grain size and temperature dependencies for interpretations and extrapolations. (a) n-value calculations based on mostly Type III experiments. Assumptions and extrapolations see text. Arrow in grey indicates that this Type II experiment did not reach steady state stress yet and therefore might continue to weaken. Furthermore, its strain rate is a minimum value, however, localization might mean strain rates to up to $10^{-4}s^{-1}$. (b) Minimum and maximum grain size dependency taken at the points marked with a cross in (a). (c) Temperature dependence/activation energy calculations based on the pentagon points in (a), taking into account several experiments and experimental data points. Verification of calculated parameters in Supplementary.

3.2 Stress - strain rate dependence (stress exponent *n*)

To compile the dependence of stress on strain rate we used data from strain rate stepping (Type III) and localized shear experiments (Type I), grouping them by grain size and temperature. The $\log_{10}$ of the differential stress (friction corrected) is

275 plotted against the $\log_{10}$ of equivalent strain rate (calculated with the shear zone angle and shear zone width; Fig. 6). A slope for each group was calculated by linear regression. The given error is based on the misfit of the regression line. As can be seen from Fig. 4, especially Type II experiments are very consistent with each other. The slopes defining the stress-strain rate relationship are based on the stepping experiments of Type III and can be fitted reasonably (Fig. 6). The slope calculated from Type III stepping experiments was used to construct the slopes for the single-value experiments of Type I and II.

280 For fine-grained experiments, we obtain $n=1.47\pm0.17$ at 650°C and $n=1.40\pm0.17$ at 725°C (Fig. 6). In the case of our polymineralic samples, Type I and Type III experiments are very valuable to understand the deformation mechanisms in polymineralic rocks. However, the geometries and boundary conditions induce a large error in the stress measurements. On the other hand, the Type II experiments have a well constrained geometry and show more consistent mechanical data (Fig. 4). By combining data sets of all experiments, we try to improve the interpretations of deformation mechanisms based on observed

285 microstructures and mechanical data and improve corrections to build a better dataset for extrapolations.

For coarse-grained experiments of Type III at 650°C, a stress exponent of $n=1.81\pm0.17$ has been calculated. This differs from the previously observed and consistently reported value of $n=1.4$ to 1.47. The discrepancy in the calculated stress exponent is attributed to the microstructural variations and the presence of bimodal grain size distributions, as detailed in the companion paper 1. Consequently, this stress exponent is not incorporated into the flow law. The influence of grain sizes on the observed

290 stresses and strain rates will be elaborated upon in section 4.3.

3.3 Grain size dependence (grain size exponent *m*)

As previously described, experiment Type I shows a grain size reduction and strain localization evolution (Fig. 5, section 3.1), which was used to calculate a grain size exponent *m* (Fig. 6). At peak stress, the shear zone width and corresponding grain sizes are well defined (Fig. 5a). These grain sizes and strain rates also correlate well with the grain sizes and strain rates

295 measured in experiment Type III fine-grained. Subsequently, strain localization occurred accompanied by weakening towards a more steady state stress. In the microstructures, we differentiate two types of shear zones gradually evolving and deforming at different strain rates: (1) a 2 µm wide zone with grain sizes of 50 nm (Fig. 5b) as well as (2) a 200 nm wide zone with grain sizes of 13 nm (Fig. 5c). It is not clear, whether both zones are active at the steady state stress or only the second, very localized zone (see discussion in companion paper 1). Hence, we evaluate the range of the grain size exponent based on these two

300 endmembers. The resulting exponent lies between $m = 0.99$ and 2.33, which is a large range indicating a huge uncertainty (see Fig. 6). This uncertainty is not surprising given the crude data set due to natural sample inhomogeneities. In the following we

assume an average $m = 1.66$. Still, it is to be noted that the values and range are lower than the $m = 3$ predicted for grain boundary diffusion-controlled grain size sensitive (=GSS) creep.

3.4 Temperature dependence (activation energy Q)

305 In order to approximate a flow law (Eq. 4), also a temperature-dependent activation energy needs to be calculated. We have only very limited data that is insufficient to directly calculate the slopes of the Q values from $1/T$ versus $\log_{10}$(differential stress) diagrams. Therefore, we use the interpolated lines for fine-grained samples at 650 and 725°C at an equivalent strain rate of 10^{-3}s^{-1} (see Fig. 6a,c). These are the most reliable data of our data set, even though the temperature difference is rather small (Fig. 6). The used fit connects only two data points, so that it can only be considered as a rough and preliminary estimate.

310 However, as it is a regression through several experiments, the two data points contain more convincing data than just two points from two directly compared experiments would have. Taking into account the large error on the value, uncertainties of the temperature (as for example in Tullis and Yund (1977)) are negligible.

The resulting $Q \sim 167$ kJ/mol is not consistent with previous experimental results of $Q=16$ kJ/mol (Sun and Pec, 2021) for nanocrystalline granitoid material, but lies more in the range of activation energies for feldspar diffusion creep $Q = 170$kJ/mol

315 (Rybacki and Dresen, 2000).

3.5 The rest (pre-exponential term A)

Table 2: Calculated flow law parameters from our experiments. The largest uncertainty comes from the grain size exponent m, also leading to different A parameters. We show a minimum, maximum and average m-value.

n	m	Q (kJ/mol)	A (MPa^{-n} µm^m s^{-1})
1.47	0.99	167.418	124.81
1.47	2.33	167.418	19.55
1.47	**1.66**	**167.418**	**49.40**

320 The A value is calculated from solving Eq. 4 for A and averaging over all our input experiments. For such a procedure, the flow law can be obtained for the experimental data set (see verification in supplementary). The largest uncertainties lie in the m- and Q-values, which result in different A-values of $A_{m0.99}=124.81$ MPa^{-n} µm^m s^{-1} and $A_{m2.33}=19.55$ MPa^{-n} µm^m s^{-1} for the given Q-value of 167 kJ/mol (see Table 2). Thus, we have to consider an uncertainty in A of at least one order of magnitude.

4 Discussion

325 We performed experiments on fine-grained granitic ultramylonites in a temperature range of 650-725°C and strain rates $\dot{\gamma}$ = 10^{-6}-10^{-3} s^{-1} in three different experimental set-ups and with varying grain sizes (see Table 2). We obtained stress exponents ($n \approx 1.5$) and grain size exponents ($m = 0.99$ to 2.33) indicating grain size sensitive deformation mechanisms in our experimental range and fitted Q and A values to obtain a first-order guess of flow law parameters for granitoid mylonites (equation 3). The purpose of this approach is to compare our results with other studies and try to extrapolate the experimental

330 observations to natural tectonic rates and -settings.

We have shown that granitic fine-grained rocks deform through grain size sensitive creep (GSS) at experimental conditions of relatively low temperature (650°C) and fast strain rates ($\dot{\gamma}$ of up to 10^{-3} s^{-1}).

4.1 Comparison with literature and extrapolation

335 Conventionally, quartz is assumed to be the weakest mechanical phase in the middle crust. Therefore, many numerical studies on the rheology of the Earth's crust use quartz flow laws as a first order approximation (Afonso and Ranalli, 2004; Burov and Watts, 2006; Fossen, 2016; Ranalli and Murphy, 1987; Schmalholz and Duretz, 2015). However, direct comparison with our and previous experiments shows that at the chosen experimental T and $\dot{\gamma}$ conditions, monomineralic quartz is considerably stronger than samples of polymineralic granitoid or monomineralic feldspar compositions, if flow law parameters are

340 calculated for our experimental conditions (Fig. 7).

For example, the presented quartz/novaculite experiments are all stronger than our fine-grained granitoids, even at µm-grain sizes (Fig. 7). In all of these quartz experiments, a brittle/frictional component is observed (because of the imposed strain rates at low temperatures). In addition, deformation by grain size insensitive (GSI) creep is inferred. Both aspects explain the strong behaviour of the tested quartz samples. (Wet) quartzite is deformed in a partially frictional manner at experimental

345 temperatures below 700°C at experimental strain rates of ~ 10^{-5} to 10^{-6} s^{-1} (Richter et al., 2018). At >800°C, fine-grained quartzite is fully viscous at strain rates of ~ 10^{-5} to 10^{-6} s^{-1} and deforms by a combination of dislocation glide and recovery by dissolution-precipitation processes including grain boundary sliding processes (Fukuda et al., 2018; Ghosh et al., 2023, 2024).
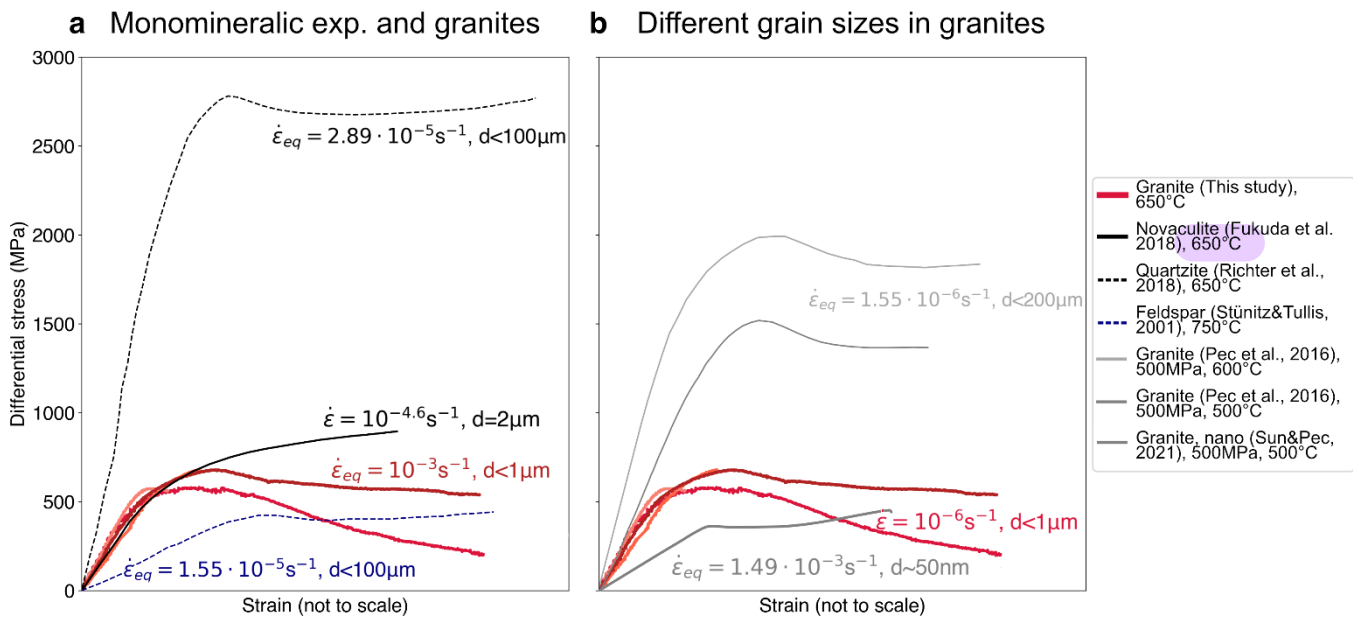
Figure 7: Direct comparison of our experiments with different materials at similar experimental conditions. Since pure shear and simple shear experiments are compared and our experiments reach much higher γ values, the x-axis is not to scale, and we compare just the differential stresses among the different studies. The corresponding grain sizes and strain rates are noted next to the stress strain curves. (a): Comparison with monomineralic quartz and feldspar, where our fine-grained granite experiments are much weaker than coarse quartz, while feldspar at higher temperatures is comparably weak. (b): Comparison of different granite experiments with different grain sizes highlighting the grain size effect on the strength.

In contrast, the deformation mechanism in our polymineralic granitoid samples at considerably lower temperatures of 650°C

350 is completely viscous (see companion paper 1), and the active GSS creep mechanisms render our samples considerably weaker than quartzites (Fig. 7). Furthermore, the grain size sensitivity of polymineralic rocks is highlighted by comparing experimental studies of granites with different grain sizes to our ultramylonites (Fig. 7, (Pec et al., 2016; Sun and Pec, 2021)). It is to be noted that our experiments are faster than many other experimental studies, underlining the strength difference between studies and the strong relationship of grain size and strain rate for strength.

355 There are not many studies performed at lower temperatures (<750°C) but high confining pressures (>1 GPa) on quartz/quartzite or feldspars because below these temperatures, at experimental strain rates, brittle behaviour was observed (Pec et al., 2016; Richter et al., 2018). Hence, the fact that our deformed polymineralic granitoid samples allow for dominantly viscous deformation at such low temperatures indicates that their mechanically weak character originates from the very small grain sizes obtained during early stages in the experiment. For any direct comparison with literature in terms of mechanical

360 data it is therefore important to keep in mind the different experimental setups, corrections applied on recorded data, and the resulting grain sizes and strain rates in experiments.

To account for the experimental differences, we compare experimental studies in more detail by extrapolating already existing flow laws (see Table 3) to conditions of our experiments (see Fig. 8). There are no studies showing GSS creep at experimental strain rates and "low" temperatures of 650°C in quartz at differential stresses <1000 MPa. The GSS and GSI quartz flow laws

365 of Rutter and Brodie, 2004a, b are widely used, but their data overestimates crustal strength and does not show viscous deformation at temperatures of 300°C, where it is observed in nature (as shown by e.g. Ghosh et al., 2022). Therefore, we focus our comparisons with quartz (Figs. 8, 9) on the most commonly used dislocation creep flow law of Hirth et al. 2001 and the up to this date weakest quartz flow law, which also includes a grain size sensitivity (Fukuda et al., 2018), as well as a GSS flow law of feldspar in Fig. 8, 9.

370 **Table 3: Flow law parameters of studies we used to compare rheological behaviour.** n = stress exponent, $-m$ = grain size exponent, r = fugacity exponent (for water) (see equation 4).

| Material	Water (wt%)	Deformation mechanism	n	$-m$	Q (kJ/mol)	log A (MPa^{-n} µm^m s^{-1})	r	Reference
Simpson quartzite	?	Dislocation creep	4	0	135+/-15	11.2+/-0.6	1	Hirth et al., 2001
Tana quartzite	as-is/ 0.1	Dislocation creep	2	0	110	log(1.56·10^{-9})	1	Ghosh et al., 2022
Novaculite	0.1-0.2	Dislocation & Diffusion creep	1.7+/-0.2	0.51+/-0.13	183+/-25	log(10$^{-2.97+/-0.23}$)	1.0 +/-0.2	Fukuda et al., 2018
Anorthite (an100)	0.07	Diffusion creep	1.0+/-0.1	3	170+/-6	1.7+/-0.2	—	Rybacki and Dresen, 2000
Anorthite (an100)	0.07	Dislocation creep	3.0+/-0.2	0	356+/-9	2.6+/-0.3	—	Rybacki and Dresen, 2000
Granitic ultramylonite	0.1-0.2	P-DPC	1.47	1.66	167	log(49.40)	—	This study
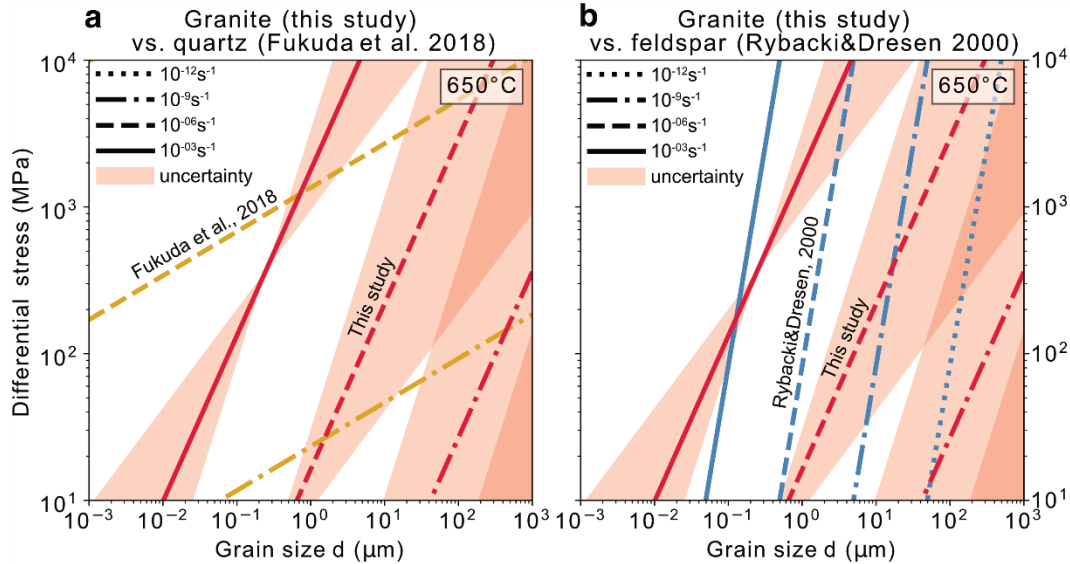
Figure 8: Comparison of quartz (a) and feldspar (b) flow laws with our experiments at 650°C with variable strain rates. It is to be noted that the flow law of Fukuda et al. (2018) (a) has a much lower grain size sensitivity, but there are intersection points, where at a larger grain size, but same grain size Fukuda et al. (2018) would be weaker than this study. Still, this study is mostly weaker than Fukuda et al. (2018) at fine grain sizes and same strain rates (a). The Rybacki and Dresen (2000) feldspar diffusion creep, however, and this studies granitoid are very similar (b). This studies granitoid appears slightly weaker at the same grain sizes and strain rates, but this difference may lie within the uncertainty of the flow law calculations. For more discussion, see text.

In GSI quartz flow laws, an additional fugacity term $f_{H_2O}^r$ exists, with *r* being the fugacity exponent, which is also implemented

in the plots below (see Table 3). The flow law from equation 4 changes then to $\dot{\varepsilon}_{eq} = A\,\sigma^n d^{-m} f_{H_2O}^r exp^{(-Q/_{RT})}$, and if there

is no grain size sensitivity: *m = 0* and therefore $d^{-m} = 1$. It is to be noted, that it has been shown by Ghosh et al. 2022 that fine-grained novaculite is weaker than coarse grained quartzite, thereby proving that, even though not directly implemented in the same form of flow law, a grain size sensitivity exists.

For our fine-grained experiments, we use the best constrained *n = 1.47*. This value is neither consistent with classical *n = 1* for GSS creep nor with *n = 3* for GSI creep (Coble, 1963; Herring, 1950; Nabarro, 1948; Rutter and Brodie, 2004a; Rybacki and Dresen, 2000). However, similar stress-strain rate sensitivities have been observed in microcrystalline quartz/novaculite (Fukuda et al., 2018; Ghosh et al., 2022, 2023, 2024; Richter et al., 2018) or nanocrystalline granites (Sun and Pec, 2021). Our grain size exponent has a wide range of *m = 0.99* to *2.33*. The smallest value indicates a linear grain-size sensitivity, that is not expected for GSS creep (Rutter and Brodie, 2004a; Rybacki and Dresen, 2000), but similar values have been obtained by Fukuda et al., 2018 and Richter et al., 2018. In order to use an intermediate value of our *m*-value range, we use *m = 1.66* and the corresponding *A* value (see Table 2 for our extrapolations in Figs. 8-10).

Extrapolation from quartz flow laws to 650°C (Fig. 8) highlights once more that the deformation through GSS creep occurs in quartz at order of magnitudes slower strain rates than observed in our granitoid samples. GSS creep in feldspars (Rybacki and Dresen, 2000), however, appears to occur at similar conditions to our granitoid fine-grained samples at the given temperatures.

390 When extrapolated to nature, these temperature and pressure conditions (650-725°C, ~1GPa) correspond to amphibolite facies metamorphic conditions. Amphibolite conditions have been reported in many tectonic settings (e.g. Ceccato et al., 2022; Goncalves et al., 2016; Imon et al., 2002; Pennacchioni and Mancktelow, 2007). We can confirm that many field observations compare well with those of our microstructures and observed deformation mechanisms (see companion paper 1). Hence, we can apply the implications from the mechanical data to constrain stresses and strain rates of fine-grained, polymineralic, viscous

395 shear zones forming in amphibolite conditions, particularly for fast deformation conditions such as carried out in our experiments.

We can confirm through the mechanical data that shear zones in polymineralic rocks at these conditions will localize in precursor structures that have reduced the grain size initially (e.g. Fitz Gerald and Stünitz, 1993). Granitoid rocks deform viscously in the lower to middle crust, after an uplift, brittle overprint at the surface might occur and vice versa, and brittle

400 fractures can serve as precursors for viscous deformation. This cyclic deformational behaviour related to burial and uplift of the crust may be common, leading to mesoscopic inhomogeneities in the rock that can serve as weak zones to localize strain (Fitz Gerald et al., 2006; Mancktelow and Pennacchioni, 2005; Pennacchioni and Mancktelow, 2007). It has been shown that even in a freshly formed granite not undergoing any previous deformation cycle there are mesoscopic local inhomogeneities/precursors that can localize strain and weaken the rock (Pennacchioni and Mancktelow, 2007). The operating

405 process that causes the initial weakening is the micro-scale comminution of grains, which is most efficient in feldspars (Fitz Gerald and Stünitz, 1993; Keulen et al., 2007; Tullis and Yund, 1985).

Although in our experiments a precursor fracture (Type I) or existing shear zone (Type III) is necessary to localize the strain, we can infer that a mylonite such as our experimental starting material inside a coarse host rock may be sufficient to activate the same processes we observe in the experiments and thereby localize strain within. A key to localize strain is therefore the

410 rheological contrast between host rock and shear zone. Overall, the grain size reduction is far less efficient in Type II samples and therefore the GSS deformation mechanisms initiate less efficiently. This information is important to understand the evolution of natural shear zones and applicability of our experiments.

Once the grain size is reduced, polymineralic fine-grained zones will deform through GSS creep and as a result will be weaker than quartz and the surrounding coarse-grained rocks. One likely micromechanical mechanism of the GSS creep is dissolution

415 precipitation creep (DPC) The processes of DPC in feldspars in granitoid systems are already reported from nature (e.g. Menegon et al., 2008). Further, we infer that at very fine grain sizes such polymineralic shear zones can deform viscously by very fast strain rates (up to $10^{-2}s^{-1}$ at 650°C, as in our experiments). The combination of weak zones localizing the strain and the very fast deformation rates explains how the lower to middle granitoid crust (~10 km depth) can be deforming in very

narrow localized shear zones rather than distributed homogeneously (e.g. Wehrens et al., 2016). By current geophysical
420   monitoring devices, detection of strain rates at sufficient spatial resolution at depths of amphibolite conditions is not possible.
However, the occurrence of slow slip events and seismicity at these depths may indicate that our new mechanical data might
be highly relevant for such conditions, and potentially even contribute to an improved parameterization of the seismic cycle.
Our experimental samples may not have reached steady state microstructures yet, especially as observed in Type II and Type
III-coarse grained samples. If grain comminution continues, the shear zone is expected to become weaker with progressive
425   strain (=increasing the strain rate at constant load). This progression might lead to acceleration of slip movement of shear zones
at mid-crustal conditions at comparable P/T and strain rates to our experiments, as well as upscale to shallower and colder
levels, representing the brittle to viscous transition. At the tips of the shear zones, stress concentrations will develop, causing
more grain comminution by potentially brittle processes (Pec et al., 2016) and leading to seismic rupture.

Further, we extrapolate the flow laws to natural strain rates of $10^{-12}s^{-1}$ and investigate the flow strengths of various deformation
430   mechanisms with temperature as a proxy of depth (Fig. 9). For fugacity calculations in GSI creep (Fig. 9a) (implementing code
from Tony Withers Fugacity Calculator, https://publish.uwo.ca/~awither5/fugacity/index.htm) we assume a lithostatic pressure
increase (density of 2.7g/cm^3) together with a temperature gradient of 25°C/km.
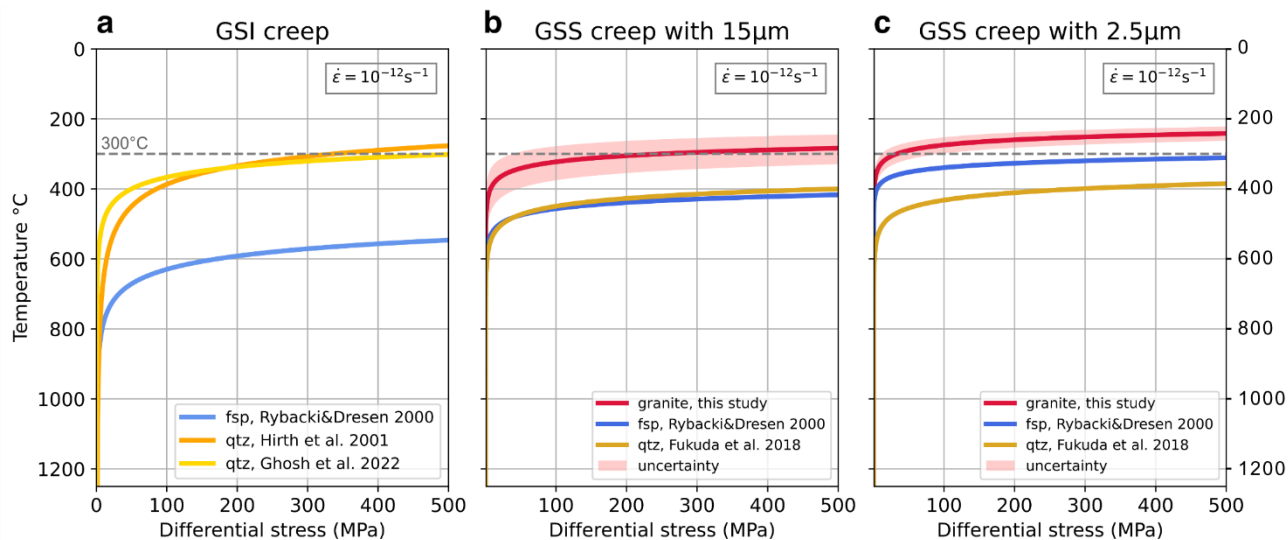

**Figure 9: Comparison of deformation mechanisms of qtz, fsp and granite at common viscous strain rates of $10^{-12}s^{-1}$. (a) is GSI
creep, where quartz is the weakest rheology, (b and c) show GSS creep with 15 and 2.5 µm, where fsp and granite become
weaker than quartz GSS with 15 µm and even weaker than qtz GSI creep at 2.5 µm. The 300°C line across all plots points at
the observed onset of GSS creep in nature. References as in Fig. 9.**

We extrapolate GSS creep to grain sizes of 15 µm (Fig. 9b), just as observed in our starting material and other common fault
rocks/ultramylonites. Further we extrapolate GSS creep also to an even finer grain size of 2.5 µm (Fig. 9c), as can be observed
435   in other ultramylonitic shear zones (Hiraga et al., 1999; Kerrich et al., 1980) or shear zones with precursor pseudotachylites

(Menegon et al., 2017) or cataclasites (Takagi et al., 2000). Furthermore, it cannot be excluded that deformation in nature occurs at finer grain sizes than preserved today, due to post-deformational static recrystallization or grain coarsening (Evans et al., 2001; Heilbronner and Tullis, 2002). We assume strain rates and differential stresses as reported from natural shortening rates/shear zones (10^{-12} s^{-1}, 300 MPa) for extrapolations. Key observation is that while quartz GSI creep is active at 300°C

440 (Fig. 9a) – feldspar and granitoid GSS creep with a significantly small grain size becomes active as well and even weaker than the quartz (Fig. 9b,c).

Still, at larger grain sizes than 15 μm, especially coarse undeformed granites with grain sizes of >1 mm, will be stronger than quartz. We therefore investigate the transition from quartz GSI to feldspar/granitoid GSS creep in a conceptual, two-phase deformation mechanism map (Fig. 10). Usually, in these grain size vs. stress maps, different deformation regimes for one

445 material are plotted (as in e.g. Rybacki and Dresen, 2004). We assume that in a granitic rock, taken as the deforming material, different deformation regimes will be active, that are dependent on the grain size and switch the dominant mechanisms also between minerals.

Based on this concept (Fig. 10), we propose two different paths of shear zone formation and flow strength in polymineralic rocks: (1) With large starting grain sizes, quartz GSI creep is the rheology dominating mechanism. GSI creep will result in

450 grain size reduction with continuous deformation. The fine-grained polymineralic mixture will reach the transition grain size (e.g. 10 μm at strain rates 10^{-12} s^{-1}) and move into the GSS creep regime, where dissolution and precipitation creep will be active and lead to very weak flow stresses. The polymineralic mixture will lead to inhibited grain growth through pinning. (2) A shear zone, which has already grain sizes which are in the grain size sensitive field in the diagram (Fig. 10) will directly deform through GSS (dissolution and precipitation) creep. Larger grains in this mixture might still deform through GSI (e.g.

455 dislocation creep/glide), but also there, grain size reduction combined with phase mixing will finally lead to a fine-grained, homogeneously deforming, weak shear zone. The microstructural evolution is described in more detail in companion paper 1.
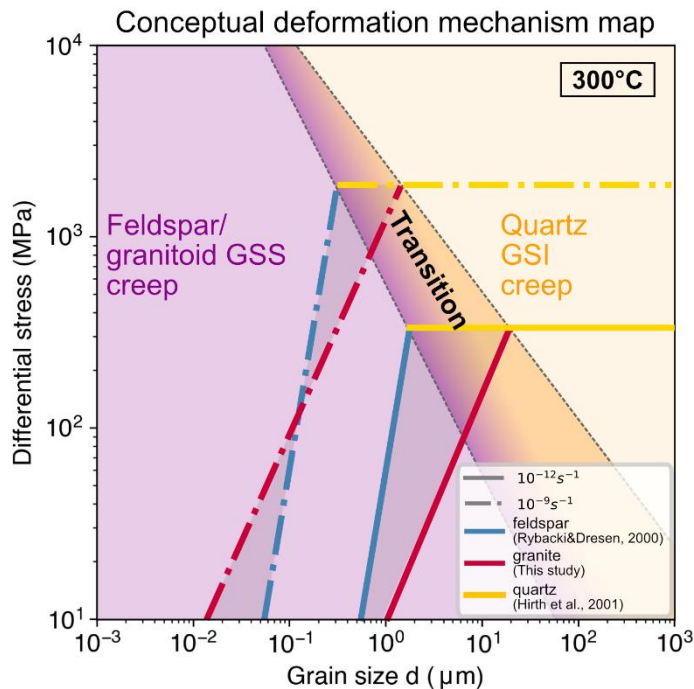
Figure 10: Conceptual model for deformation in granitoid rocks. We infer that in granitoid rocks, not only the deformation mechanism but also the deforming material will change. At strain rates of $10^{-12}s^{-1}$ the deformation will be dominated by quartz GSI creep in grain sizes above 10 μm, and transition into GSS creep in the polymineralic mixture of feldspars and biotite (DPC).

Most evidence in nature is found for concept (2), as in e.g. Goncalves et al. (2016); Imon et al. (2002); Kilian et al. (2011); Menegon et al. (2017); Stokes et al. (2012). However, in our Type II experiments, we already observe that the grain size reduction and phase mixing (as described in companion paper 1) leads to substantial weakening in the mylonite (see Fig. 4).

460 As in Tullis and Yund (1992, 1985), a high content of feldspar is expected to contribute to weakening, but in addition also reactions of feldspars, forming stable minerals at the conditions of deformation (Fitz Gerald and Stünitz, 1993; Mansard et al., 2020a, b; Marti et al., 2017, 2018; Stünitz and Fitz Gerald, 1993).

If only the reaction kinetics are the driving forces for the low stresses and efficient grain size reduction, an important question remains, whether our experimental observations and flow law parameters could be transferred to shallower depths and lower

465 temperatures than the experimental conditions. Here we assume that at almost all P,T-conditions, be it lower or higher than the peak metamorphic conditions of the rock, phases such as feldspars or biotites will be in a disequilibrium. This chemical disequilibrium will enhance the efficiency of pressure solution (e.g. Stünitz et al., 2020). Hence, the extrapolation of the observed microstructures and interpretation is possible beyond greenschist facies and experimental conditions.

The consequences of the calculated flow law is very similar to that of Rybacki and Dresen (2000) GSS (diffusion) creep of

470   wet anorthite, even though the individual flow law parameters, other than Q, differ (see Table 3, Fig. 8). This leads to the impression that feldspar as the dominant phase in our samples might be the material defining the rheology. There have been studies implying that reactions in at least two types of feldspars would enhance reactivity in rocks and thereby weaken the rock through activation of GSS creep (Fitz Gerald and Stünitz, 1993; Mansard et al., 2020a, b; Marti et al., 2017, 2018; Stünitz and Fitz Gerald, 1993; Stünitz and Tullis, 2001; Tullis et al., 1990). This means that if feldspar is dominating the composition in

475   the rock, at a given grain size feldspars would become the weakest and rheology defining phases. We cannot exclude this important contribution of the feldspar minerals on the rheology of our samples.

However, based on the microstructural observations in our samples (see companion paper 1), we still infer that, although the feldspar flow law appears a good approximation for the rheology in polymineralic fine-grained granitoids, a feldspar GSS creep flow law would be an oversimplification. The polymineralic mixture allows the (feldspar) grain size to remain small and

480   active at or even below the boundary between GSI and GSS creep through phase mixing, chemical driving forces, and pinning. The microstructures indicate that the deformation through reactions is weakening the rock even further, (1) allowing for the activation of pinning-assisted dissolution and precipitation creep (DPC) (companion paper 1), and (2) possibly enhancing the deformation. Therefore, the presented flow law parameters might overestimate the strength in granitoid (fault) rocks.

The uncertainty of parameters estimated in this study is high, due to a limited number of experiments at different steady state

485   flow stresses, different corrections applied between each experiment, and inhomogeneities in the natural starting material. However, the complexity of observations from our experiments is important, as monomineralic microstructures are different to polymineralic. This is why further experiments with complex systems as these are necessary to understand the rheology of polymineralic mylonites. It is important to investigate the influence of water content on the pinning-assisted DPC processes. Furthermore, the influence of volumetric proportion of feldspars and biotite versus quartz on the dominant deformation

490   mechanism is still not understood and could be modified in future experiments.

4.2 Pure shear samples – Type II experiments and flow law

For the flow law calculations, we did not use any of the Type II experiments. However, the minimum strain rate and minimum

495   stress of experiment 670NN is plotted in the same stress-strain rate diagram as the experiments used for the calculations above (Fig. 6). Although it does not appear to fit with our other experimental datasets, it is to be considered that the grain sizes in this experiment have a large range and that local strain rates (of material with different sizes) may be orders of magnitudes faster, if we assume only phase boundaries to deform (by grain boundary sliding). The arrow is also indicating that weakening is still continuing (see mechanical data Fig. 4), assuming that the grain size reduction in these experiments is still on-going. In

500   this sense, the microstructural and mechanical evolution is in line with the observations made by Type I and III experiments and supports those results.

4.3 Bimodal grain size distributions and "bimodal" strain rates

Figure 11: Schematic overlay of strain localization in Type III-cg experiment 675NN. SEM-BSE image of large clast from the bottom surrounded by high strain grains is displayed in Fig. 3.

It is to be noted that a change in the *n*-slope from 1.40 or 1.47 in fine grained Type III samples to *n* = 1.81±0.17 for the Type III-coarse grained sample (Fig. 6) occurs. This change in slope indicates a combination and contribution of different deformation mechanisms and must be explained by the microstructures. Initially coarse-grained samples of Type III - coarse grained samples (<125 μm) exhibit a complex microstructure with at least bimodal grain size distribution, foliation development, and strain localization in shear bands. We mapped out the different deformation domains in the sample 675NN, see Fig. 11, where we distinguish five different zones. (1) to (4) are low to medium strain features, and (5) are high strain zones with extremely reduced grain size where flow textures are similar to Type III-fine grained experiments. The bimodal grain size distribution may indicate two different deformation mechanisms that are active at the same time in the coarse- and fine-grained regions, which is in accordance with the two different n-values.

Commonly, for determining of a bulk rheology, limiting assumptions are made that either stress or strain rate are rate-limiting within an aggregate (Voigt, 1910). It has already been shown by Handy (1994) (and references therein), that such an approach is an oversimplification of the complexity of bulk rock deformation, as the stress and strain partitions differently between stronger and weaker phases. Similar composite flow law approaches were made by Herwegh et al. (2005), Ter Heege et al. (2002), where at constant stress, the bulk strain rate is a sum of each discrete group weighted by its volume:

$$\dot{\varepsilon}_\sigma = \dot{\varepsilon}_1 v_1 + \dot{\varepsilon}_2 v_2 + \cdots + \dot{\varepsilon}_j v_j = \sum_{i=1}^{i=j} \dot{\varepsilon}_i v_i \ , \tag{5}$$

And analogously, at constant strain rate the bulk stress becomes a composite of all stresses in the system:

$$\sigma_{\dot{\varepsilon}} = \sigma_1 v_1 + \sigma_2 v_2 + \cdots + \sigma_j v_j = \sum_{i=1}^{i=j} \sigma_i v_i \ , \tag{6}$$

A further complication in such a system is the progressive evolution of parameters with increasing strain leading to a change in rheology. This complication is neglected in this approach. To obtain the contribution of each grain size group/deformation mechanism in Type III-coarse grained experiments affecting the strain rate/stress we use equation 5. Under the assumption that a fine-grained zone (5) in sample Type III-cg, as in Fig. 11, can be described by Type III-fine grained experiments, and the stress is steady state in the sample, we calculate the strain rate of the coarse portion of the coarse grains. In our case we use the area-fraction instead

29

of volume fraction for the calculations. We use the strain rates of a regression line (see *n*-value slope in Fig. 6) through Type III-fine grained and Type I experiments at the corresponding stress.

535

Table 4: Calculations of contributions of fine- and coarse-grained zones strain rates at a constant stress.

Exp. No.	Bulk $\dot{\varepsilon}_{eq}$ (s^{-1})	σ_{Diff} (MPa)	Area fg (%)	Area cg (%)	Fine $\dot{\varepsilon}_{eq}$ (s^{-1})	Coarse $\dot{\varepsilon}_{eq}$ (s^{-1})
675NN	$6.99 \cdot 10^{-4}$	650	7.50%	92.50%	$1.38 \cdot 10^{-3}$	$6.43 \cdot 10^{-4}$
675NN	$6.73 \cdot 10^{-5}$	264	7.50%	92.50%	$3.79 \cdot 10^{-4}$	$4.20 \cdot 10^{-5}$
675NN	$1.31 \cdot 10^{-5}$	83	7.50%	92.50%	$6.91 \cdot 10^{-5}$	$8.56 \cdot 10^{-6}$
675NN	$5.86 \cdot 10^{-4}$	811	7.50%	92.50%	$1.96 \cdot 10^{-3}$	$4.75 \cdot 10^{-4}$

The results of these calculations (Table 4) show that the fine grain sizes that have formed only account for ~10% of the sample and thus the bulk strength and the coarse grains are still dominating the microstructure of the sample and thus the rheology.

540 However, the microstructures also indicate that the sample is not yet at steady-state conditions and the grain size reduction (and weakening) will continue at higher strains.

From *n*-calculations on the coarse-grained portion of our samples we can use the microstructural observations of the different deformation mechanisms that appear to be active at the same time: Most importantly, we observe that the coarse-grained portion of the sample 675NN has a stress exponent of *n* = 1.94 +/-0.17 (Fig. 6), supporting that the deformation mechanism in

545 this part of the sample is possibly more affected by grain size insensitive creep components (e.g. dislocation glide). This value is also comparable to the flow law parameters of Hansen and Carter (1983) for (coarse) wet Westerly granite.

Overall, in terms of strain localization and bulk rheology these coarse experiments therefore point at the fact that in coarser starting materials it becomes necessary to view at a combination of deformation mechanisms. In this sense, these Type III-cg experiments are a good analogue for deformation to higher strains of Type II experiments.

550 **5 Summary and Conclusions**

To understand the rheology of fine-grained polymineralic (fault) rocks, three different types of experiments on a granitic ultramylonite at T = 650-725°C, P$_{conf}$ = 1.2 GPa, and strain rates of $\dot{\gamma}$ = 10^{-6}-10^{-2} s^{-1} were used approximate parameters in a grain size sensitive (GSS) flow law in order to be able to compare our results to other flow parameters and in order to extrapolate to natural conditions. For fine-grained rocks we obtained $n \approx 1.5$, $m \approx -1$ to -2.3, $Q = 167$ kJ/mol, and $A =$

555 19.55(124.81) MPa^{-n} μm^{m} s^{-1}. In coarse samples, a mixed flow law in terms of deformation mechanisms describes the stress sensitivity in coarse polymineralic material well: grains larger than ~10 μm deform with a grain size insensitive (GSI) creep component ($n \approx 2$), while a fine-grained fraction deforms with grain size sensitive creep (n $\approx$ 1.5) simultaneously. The flow

law parameters have a large error and are not intended to be applied to granitoid rocks ubiquitously, but only to serve as an aid in understanding and comparing the rheology of polymineralic shear zones with other literature data.

560 In connection with microstructural observations from companion paper 1, we confirm field observations that polymineralic fine-grained rocks deform through GSS creep, (dissolution, nucleation, and growth, coupled with pinning - DPC). At amphibolite conditions, fine-grained polymineralic rocks are deforming up to six orders of magnitude faster than quartz at the same differential stress. While feldspar GSS flow laws seem to result in comparable strengths to fine-grained granitoids in this study, it is implied that pinning and chemical driving forces will aid initiating GSS creep in granitoids, showing that our

565 estimated flow law parameters might still overestimate the flow strength in fine-grained polymineralic rocks.

Further extrapolations to lower temperatures of 300°C show that grain size is key for weakening granitoid fault rocks by activating GSS creep. Until the rock reaches a fine grain size, quartz with GSI creep is still the rheology defining weakest phase (e.g. >~10 μm, coarse intact granite, at $\dot{\varepsilon} = 10^{-12}\text{s}^{-1}$). At a reduced grain size through progressive grain size reduction during deformation, the polymineralic mixture deforms by GSS creep (pinning-assisted DPC), weakening the polymineralic

570 shear zones dramatically. Onset of viscous deformation at lower temperatures implies that the brittle to viscous transition of granitoid shear zones can occur at a shallower crustal level than estimated from quartz. Further, the strain rate in localized shear zones will be underestimated, possibly explaining stress build-ups and stress concentrations in the middle crust leading to earthquakes. The latter process would represent a change from viscous deformation to brittle at stress concentrations and thus may present a potential earthquake mechanism that is a run-away process induced by viscous deformation.

575

References

590 Afonso, J. C. and Ranalli, G.: Crustal and mantle strengths in continental lithosphere: is the jelly sandwich model obsolete?, Tectonophysics, 394, 221–232, https://doi.org/10.1016/j.tecto.2004.08.006, 2004.

Tony Withers: Fugacity Calculator: https://publish.uwo.ca/~awither5/fugacity/index.htm, last access: 19 June 2024.

Arnold, J., Jacoby, W. R., Schmeling, H., and Schott, B.: Continental collision and the dynamic and thermal evolution of the Variscan orogenic crustal root Ð numerical models, Journal of Geodynamics, 2001.

595 Berger, A., Herwegh, M., Schwarz, J.-O., and Putlitz, B.: Quantitative analysis of crystal/grain sizes and their distributions in 2D and 3D, Journal of Structural Geology, 33, 1751–1763, https://doi.org/10.1016/j.jsg.2011.07.002, 2011.

Brace, W. F. and Kohlstedt, D. L.: Limits on lithospheric stress imposed by laboratory experiments, J. Geophys. Res., 85, 6248–6252, https://doi.org/10.1029/JB085iB11p06248, 1980.

Brok, B. den: An experimental investigation into the effect of water on the flow of quartzite, The effect of water on the flow
600 of quartzite, 95, https://doi.org/10.3929/ethz-a-000684352, 1992.

Burov, E. B.: The upper crust is softer than dry quartzite, Tectonophysics, 361, 321–326, https://doi.org/10.1016/S0040-1951(02)00608-X, 2003.

Burov, E. B.: Rheology and strength of the lithosphere, Marine and Petroleum Geology, 28, 1402–1443, https://doi.org/10.1016/j.marpetgeo.2011.05.008, 2011.

605 Burov, E. B. and Watts, A. B.: The long-term strength of continental lithosphere: "jelly sandwich" or "crème brûlée"?, Gsa Today, 16, 4, https://doi.org/10.1130/1052-5173(2006)016<4:TLTSOC>2.0.CO;2, 2006.

Campbell, L. R., Menegon, L., Fagereng, Å., and Pennacchioni, G.: Earthquake nucleation in the lower crust by local stress amplification, Nat Commun, 11, 1322, https://doi.org/10.1038/s41467-020-15150-x, 2020.

Ceccato, A., Goncalves, P., and Menegon, L.: On the petrology and microstructures of small-scale ductile shear zones in
610 granitoid rocks: An overview, Journal of Structural Geology, 161, 104667, https://doi.org/10.1016/j.jsg.2022.104667, 2022.

Challandes, N., Marquer, D., and Villa, I. M.: P-T-t modelling, fluid circulation, and 39Ar-40Ar and Rb-Sr mica ages in the Aar Massif shear zones (Swiss Alps), Swiss J. Geosci., 101, 269–288, https://doi.org/10.1007/s00015-008-1260-6, 2008.

Coble, R. L.: A Model for Boundary Diffusion Controlled Creep in Polycrystalline Materials, Journal of Applied Physics, 34, 1679–1682, https://doi.org/10.1063/1.1702656, 1963.

615 Dell'Angelo, L. N. and Tullis, J.: Experimental deformation of partially melted granitic aggregates, J Metamorph Geol, 6, 495–515, https://doi.org/10.1111/j.1525-1314.1988.tb00436.x, 1988.

Edwin, G., Daniel, K., and Urs, E.: Elelectrodynamic disaggregation of geologic material., 2006.

Evans, B., Renner, J., and Hirth, G.: A few remarks on the kinetics of static grain growth in rocks, Int J Earth Sci, 90, 88–103, https://doi.org/10.1007/s005310000150, 2001.

620 Fitz Gerald, J. D. and Stünitz, H.: Deformation of granitoids at low metamorphic grade. I: Reactions and grain size reduction, Tectonophysics, 221, 269–297, https://doi.org/10.1016/0040-1951(93)90163-E, 1993.

Fitz Gerald, J. D., Mancktelow, N. S., Pennacchioni, G., and Kunze, K.: Ultrafine-grained quartz mylonites from high-grade shear zones: Evidence for strong dry middle to lower crust, 2006.

Fossen, H.: Structural Geology, Cambridge University Press, https://doi.org/10.1017/9781107415096, 2016.

625 Fukuda, J., Holyoke III, C. W., and Kronenberg, A. K.: Deformation of Fine-Grained Quartz Aggregates by Mixed Diffusion and Dislocation Creep, Journal of Geophysical Research: Solid Earth, 123, 4676–4696, https://doi.org/10.1029/2017JB015133, 2018.

Ghosh, S., Stünitz, H., Raimbourg, H., and Précigout, J.: Quartz rheology constrained from constant-load experiments: Consequences for the strength of the continental crust, Earth and Planetary Science Letters, 597, 117814, 630 https://doi.org/10.1016/j.epsl.2022.117814, 2022.

Ghosh, S., Stünitz, H., Raimbourg, H., and Précigout, J.: Rheology and Deformation Processes of Fine-grained Quartz Aggregate, EGU23, Vienna, Austria, event-title: EGU23DOI: 10.5194/egusphere-egu23-15832, https://doi.org/10.5194/egusphere-egu23-15832, 2023.

Ghosh, S., Stünitz, H., Raimbourg, H., Précigout, J., Di Carlo, I., Heilbronner, R., and Piani, L.: Importance of grain boundary 635 processes for plasticity in the quartz-dominated crust: Implications for flow laws, Earth and Planetary Science Letters, 640, 118767, https://doi.org/10.1016/j.epsl.2024.118767, 2024.

Gleason, G. C. and Tullis, J.: A flow law for dislocation creep of quartz aggregates determined with the molten salt cell, Tectonophysics, 247, 1–23, https://doi.org/10.1016/0040-1951(95)00011-B, 1995.

Goncalves, P., Oliot, E., Marquer, D., and Connolly, J. A. D.: Role of chemical processes on shear zone formation: an example 640 from the Grimsel metagranodiorite (Aar massif, Central Alps): SHEAR ZONE FORMATION, Journal of Metamorphic Geology, 30, 703–722, https://doi.org/10.1111/j.1525-1314.2012.00991.x, 2012.

Goncalves, P., Poilvet, J.-C., Oliot, E., Trap, P., and Marquer, D.: How does shear zone nucleate? An example from the Suretta nappe (Swiss Eastern Alps), Journal of Structural Geology, 86, 166–180, https://doi.org/10.1016/j.jsg.2016.02.015, 2016.

Gratier, J.-P., Dysthe, D. K., and Renard, F.: The Role of Pressure Solution Creep in the Ductility of the Earth's Upper Crust, 645 in: Advances in Geophysics, vol. 54, Elsevier, 47–179, https://doi.org/10.1016/B978-0-12-380940-7.00002-0, 2013.

Handy, M. R.: Flow laws for rocks containing two non-linear viscous phases: A phenomenological approach, Journal of Structural Geology, 16, 287–301, https://doi.org/10.1016/0191-8141(94)90035-3, 1994.

Hansen, F. D. and Carter, N. L.: Semibrittle Creep Of Dry And Wet Westerly Granite At 1000 MPa, The 24th U.S. Symposium on Rock Mechanics (USRMS), ARMA-83-0429, 1983.

650 Heilbronner, R. and Keulen, N.: Grain size and grain shape analysis of fault rocks, Tectonophysics, 427, 199–216, https://doi.org/10.1016/j.tecto.2006.05.020, 2006.

Heilbronner, R. and Tullis, J.: The effect of static annealing on microstructures and crystallographic preferred orientations of quartzites experimentally deformed in axial compression and shear, SP, 200, 191–218, https://doi.org/10.1144/GSL.SP.2001.200.01.12, 2002.

655 Heilbronner, R., Stunitz, H., Précigout, J., and Raimbourg, H.: The solid medium deformation apparatus – reloaded, , https://doi.org/10.5194/egusphere-egu2020-9859, 2020.

Herring, C.: Diffusional Viscosity of a Polycrystalline Solid, Journal of Applied Physics, 21, 437–445, https://doi.org/10.1063/1.1699681, 1950.

Herwegh, M., de Bresser, J. H. P., and ter Heege, J. H.: Combining natural microstructures with composite flow laws: an
660 improved approach for the extrapolation of lab data to nature, Journal of Structural Geology, 27, 503–521, https://doi.org/10.1016/j.jsg.2004.10.010, 2005.

Hiraga, T., Nagase, T., and Akizuki, M.: The structure of grain boundaries in granite-origin ultramylonite studied by high-resolution electron microscopy, Physics and Chemistry of Minerals, 26, 617–623, https://doi.org/10.1007/s002690050226, 1999.

665 Hirth, G. and Tullis, J.: Dislocation creep regimes in quartz aggregates, Journal of Structural Geology, 14, 145–159, https://doi.org/10.1016/0191-8141(92)90053-Y, 1992.

Hirth, G., Teyssier, C., and Dunlap, J. W.: An evaluation of quartzite flow laws based on comparisons between experimentally and naturally deformed rocks, Int J Earth Sci, 90, 77–87, https://doi.org/10.1007/s005310000152, 2001.

Holyoke, C. W. and Kronenberg, A. K.: Accurate differential stress measurement using the molten salt cell and solid salt
670 assemblies in the Griggs apparatus with applications to strength, piezometers and rheology, Tectonophysics, 494, 17–31, https://doi.org/10.1016/j.tecto.2010.08.001, 2010.

Imon, R., Okudaira, T., and Fujimoto, A.: Dissolution and precipitation processes in deformed amphibolites: an example from the ductile shear zone of the Ryoke metamorphic belt, SW Japan, Journal Metamorphic Geology, 20, 297–308, https://doi.org/10.1046/j.1525-1314.2002.00367.x, 2002.

675 Kerrich, R., Allison, I., Barnett, R. L., Moss, S., and Starkey, J.: Microstructural and chemical transformations accompanying deformation of granite in a shear zone at Miéville, Switzerland; with implications for stress corrosion cracking and superplastic flow, Contr. Mineral. and Petrol., 73, 221–242, https://doi.org/10.1007/BF00381442, 1980.

Keulen, N., Heilbronner, R., Stünitz, H., Boullier, A.-M., and Ito, H.: Grain size distributions of fault rocks: A comparison between experimentally and naturally deformed granitoids, Journal of Structural Geology, 29, 1282–1300,
680 https://doi.org/10.1016/j.jsg.2007.04.003, 2007.

Kilian, R., Heilbronner, R., and Stünitz, H.: Quartz grain size reduction in a granitoid rock and the transition from dislocation to diffusion creep, Journal of Structural Geology, 33, 1265–1284, https://doi.org/10.1016/j.jsg.2011.05.004, 2011.

Kohlstedt, D. L. and Hansen, L. N.: Constitutive Equations, Rheological Behavior, and Viscosity of Rocks, in: Treatise on Geophysics, Elsevier, 441–472, https://doi.org/10.1016/B978-0-444-53802-4.00042-7, 2015.

685 Kohlstedt, D. L., Evans, B., and Mackwell, S. J.: Strength of the lithosphere: Constraints imposed by laboratory experiments, J. Geophys. Res., 100, 17587–17602, https://doi.org/10.1029/95JB01460, 1995.

Mancktelow, N. S. and Pennacchioni, G.: The control of precursor brittle fracture and fluid–rock interaction on the development of single and paired ductile shear zones, Journal of Structural Geology, 27, 645–661, https://doi.org/10.1016/j.jsg.2004.12.001, 2005.

690 Mansard, N., Stünitz, H., Raimbourg, H., Précigout, J., Plunder, A., and Nègre, L.: Relationship between microstructures and resistance in mafic assemblages that deform and transform, Solid Earth, 11, 2141–2167, https://doi.org/10.5194/se-11-2141-2020, 2020a.

Mansard, N., Stünitz, H., Raimbourg, H., and Précigout, J.: The role of deformation-reaction interactions to localize strain in polymineralic rocks: Insights from experimentally deformed plagioclase-pyroxene assemblages, Journal of Structural
695 Geology, 134, 104008, https://doi.org/10.1016/j.jsg.2020.104008, 2020b.

Marti, S., Stünitz, H., Heilbronner, R., Plümper, O., and Drury, M.: Experimental investigation of the brittle-viscous transition in mafic rocks – Interplay between fracturing, reaction, and viscous deformation, Journal of Structural Geology, 105, 62–79, https://doi.org/10.1016/j.jsg.2017.10.011, 2017.

Marti, S., Stünitz, H., Heilbronner, R., Plümper, O., and Kilian, R.: Syn-kinematic hydration reactions, grain size reduction,
700 and dissolution–precipitation creep in experimentally deformed plagioclase–pyroxene mixtures, Solid Earth, 9, 985–1009, https://doi.org/10.5194/se-9-985-2018, 2018.

Menegon, L., Pennacchioni, G., and Spiess, R.: Dissolution-precipitation creep of K-feldspar in mid-crustal granite mylonites, Journal of Structural Geology, 30, 565–579, https://doi.org/10.1016/j.jsg.2008.02.001, 2008.

Menegon, L., Pennacchioni, G., Malaspina, N., Harris, K., and Wood, E.: Earthquakes as Precursors of Ductile Shear Zones
705 in the Dry and Strong Lower Crust, Geochem Geophys Geosyst, 18, 4356–4374, https://doi.org/10.1002/2017GC007189, 2017.

Nabarro, F. R. N.: Deformation of Crystals by Motion of Single Ions, The Physical Society, Bristol, U.K., 1948.

Okazaki, K. and Hirth, G.: Deformation experiment on quartz aggregates with high porosity and high water contents at high pressure and temperature., American Geophysical Union Fall Meeting, 2016, Abstract T21D-2870, 2016.

710 Okudaira, T., Ogawa, D., and Michibayashi, K.: Grain-size-sensitive deformation of upper greenschist- to lower amphibolite-facies metacherts from a low-P/high-T metamorphic belt, Tectonophysics, 492, 141–149, https://doi.org/10.1016/j.tecto.2010.06.002, 2010.

Pec, M.: Experimental Investigation on the Rheology of Fault Rocks, Basel University, 210 pp., 2014.

Pec, M., Stünitz, H., and Heilbronner, R.: Semi-brittle deformation of granitoid gouges in shear experiments at elevated
715 pressures and temperatures, Journal of Structural Geology, 38, 200–221, https://doi.org/10.1016/j.jsg.2011.09.001, 2012.

Pec, M., Stünitz, H., Heilbronner, R., and Drury, M.: Semi-brittle flow of granitoid fault rocks in experiments, Journal of Geophysical Research: Solid Earth, 121, 1677–1705, https://doi.org/10.1002/2015JB012513, 2016.

Pennacchioni, G. and Mancktelow, N. S.: Nucleation and initial growth of a shear zone network within compositionally and structurally heterogeneous granitoids under amphibolite facies conditions, Journal of Structural Geology, 29, 1757–1780,
720 https://doi.org/10.1016/j.jsg.2007.06.002, 2007.

Ranalli, G. and Murphy, D. C.: Rheological stratification of the lithosphere, Tectonophysics, 132, 281–295, https://doi.org/10.1016/0040-1951(87)90348-9, 1987.

Regis, D., Rubatto, D., Darling, J., Cenki-Tok, B., Zucali, M., and Engi, M.: Multiple Metamorphic Stages within an Eclogite-facies Terrane (Sesia Zone, Western Alps) Revealed by Th–U–Pb Petrochronology, Journal of Petrology, 55, 1429–1456,
725 https://doi.org/10.1093/petrology/egu029, 2014.

Richter, B., Stünitz, H., and Heilbronner, R.: The brittle-to-viscous transition in polycrystalline quartz: An experimental study, Journal of Structural Geology, 114, 1–21, https://doi.org/10.1016/j.jsg.2018.06.005, 2018.

Rutter, E. H. and Brodie, K. H.: Experimental grain size-sensitive flow of hot-pressed Brazilian quartz aggregates, Journal of Structural Geology, 26, 2011–2023, https://doi.org/10.1016/j.jsg.2004.04.006, 2004a.

730 Rutter, E. H. and Brodie, K. H.: Experimental intracrystalline plastic flow in hot-pressed synthetic quartzite prepared from Brazilian quartz crystals, Journal of Structural Geology, 26, 259–270, https://doi.org/10.1016/S0191-8141(03)00096-8, 2004b.

Rybacki, E. and Dresen, G.: Dislocation and diffusion creep of synthetic anorthite aggregates, J. Geophys. Res., 105, 26017–26036, https://doi.org/10.1029/2000JB900223, 2000.

Rybacki, E. and Dresen, G.: Deformation mechanism maps for feldspar rocks, Tectonophysics, 382, 173–187,
735 https://doi.org/10.1016/j.tecto.2004.01.006, 2004.

Rybacki, E., Gottschalk, M., Wirth, R., and Dresen, G.: Influence of water fugacity and activation volume on the flow properties of fine-grained anorthite aggregates, J. Geophys. Res., 111, 2005JB003663, https://doi.org/10.1029/2005JB003663, 2006.

Rybacki, E., Wirth, R., and Dresen, G.: High-strain creep of feldspar rocks: Implications for cavitation and ductile failure in
740 the lower crust, Geophysical Research Letters, 35, 2007GL032478, https://doi.org/10.1029/2007GL032478, 2008.

Schmalholz, S. M. and Duretz, T.: Shear zone and nappe formation by thermal softening, related stress and temperature evolution, and application to the Alps, Journal of Metamorphic Geology, 33, 887–908, https://doi.org/10.1111/jmg.12137, 2015.

Stesky, R. M., Brace, W. F., Riley, D. K., and Robin, P.-Y. F.: Friction in faulted rock at high temperature and pressure,
745 Tectonophysics, 23, 177–203, https://doi.org/10.1016/0040-1951(74)90119-X, 1974.

Stipp, M. and Tullis, J.: The recrystallized grain size piezometer for quartz, Geophysical Research Letters, 30, https://doi.org/10.1029/2003GL018444, 2003.

Stokes, M. R., Wintsch, R. P., and Southworth, C. S.: Deformation of amphibolites via dissolution–precipitation creep in the middle and lower crust, Journal Metamorphic Geology, 30, 723–737, https://doi.org/10.1111/j.1525-1314.2012.00989.x, 2012.

750 Stünitz, H. and Fitz Gerald, J. D.: Deformation of granitoids at low metamorphic grade. II: Granular flow in albite-rich mylonites, Tectonophysics, 221, 299–324, https://doi.org/10.1016/0040-1951(93)90164-F, 1993.

Stünitz, H. and Tullis, J.: Weakening and strain localization produced by syn-deformational reaction of plagioclase, Int J Earth Sci, 90, 136–148, https://doi.org/10.1007/s005310000148, 2001.

Stünitz, H., Neufeld, K., Heilbronner, R., Finstad, A. K., Konopásek, J., and Mackenzie, J. R.: Transformation weakening:
755 Diffusion creep in eclogites as a result of interaction of mineral reactions and deformation, Journal of Structural Geology, 139, 104129, https://doi.org/10.1016/j.jsg.2020.104129, 2020.

Sun, H. and Pec, M.: Nanometric flow and earthquake instability, Nat Commun, 12, 6779, https://doi.org/10.1038/s41467-021-26996-0, 2021.

Takagi, H., Goto, K., and Shigematsu, N.: Ultramylonite bands derived from cataclasite and pseudotachylyte in granites,
760 northeast Japan, Journal of Structural Geology, 22, 1325–1339, https://doi.org/10.1016/S0191-8141(00)00034-1, 2000.

Tarantola, A., Diamond, L. W., Stünitz, H., Thust, A., and Pec, M.: Modification of fluid inclusions in quartz by deviatoric stress. III: Influence of principal stresses on inclusion density and orientation, Contrib Mineral Petrol, 164, 537–550, https://doi.org/10.1007/s00410-012-0749-1, 2012.

Ter Heege, J. H., De Bresser, J. H. P., and Spiers, C. J.: The influence of dynamic recrystallization on the grain size distribution
765 and rheological behaviour of Carrara marble deformed in axial compression, SP, 200, 331–353, https://doi.org/10.1144/GSL.SP.2001.200.01.19, 2002.

Tullis, J. and Yund, R.: Chapter 4 The Brittle-Ductile Transition in Feldspar Aggregates: An Experimental Study, in: International Geophysics, vol. 51, edited by: Evans, B. and Wong, T., Academic Press, 89–117, https://doi.org/10.1016/S0074-6142(08)62816-8, 1992.

770 Tullis, J. and Yund, R. A.: Experimental deformation of dry westerly granite, Journal of Geophysical Research (1896-1977), 82, 5705–5718, https://doi.org/10.1029/JB082i036p05705, 1977.

Tullis, J. and Yund, R. A.: Dynamic recrystallization of feldspar: A mechanism for ductile shear zone formation, Geol, 13, 238, https://doi.org/10.1130/0091-7613(1985)13<238:DROFAM>2.0.CO;2, 1985.

Tullis, J., Dell'Angelo, L., and Yund, R. A.: Ductile shear zones from brittle precursors in feldspathic rocks: The role of
775 dynamic recrystallization, in: Geophysical Monograph Series, vol. 56, edited by: Duba, A. G., Durham, W. B., Handin, J. W., and Wang, H. F., American Geophysical Union, Washington, D. C., 67–81, https://doi.org/10.1029/GM056p0067, 1990.

Voigt, W.: Lehrbuch der Kristallphysik: mit Ausschluss der Kristalloptik, B.G.Teubner, Leipzig, 1910.

Wehrens, P., Berger, A., Peters, M., Spillmann, T., and Herwegh, M.: Deformation at the frictional-viscous transition: Evidence for cycles of fluid-assisted embrittlement and ductile deformation in the granitoid crust, Tectonophysics, 693, 66–
780 84, https://doi.org/10.1016/j.tecto.2016.10.022, 2016.

Wheeler, J.: Importance of pressure solution and coble creep in the deformation of polymineralic rocks, J. Geophys. Res., 97, 4579, https://doi.org/10.1029/91JB02476, 1992.